Fat inclusions strongly alter membrane mechanics

Alexandre Santinho, Aymeric Chorlay, Lionel Foret, Abdou Rachid Thiam

Fat Inclusions Strongly Alter Membrane Mechanics.

Alexandre Santinho[1,§], Aymeric Chorlay[1,§], Lionel Foret[1], Abdou Rachid Thiam[1]*

[1] Laboratoire de Physique de l'École Normale Supérieure, ENS, Université PSL, CNRS, Sorbonne Université, Université de Paris, F-75005 Paris, France

[§] These authors contributed equally to this work

*Correspondence to:
Abdou Rachid Thiam
Laboratoire de Physique Statistique,
Ecole Normale Supérieure,
PSL Research University,
75005 Paris Cedex 05, France
thiam@ens.fr

Abstract:

Neutral lipids (NLs) are apolar oil molecules synthesized in the endoplasmic reticulum (ER) bilayer upon diverse biological stimuli. NLs synthesized are released in the hydrophobic core of the bilayer. At a critical concentration, NLs condense by phase separation and nucleate a lipid droplet (LD). After an LD forms, a fraction of NLs can be present in the bilayer but at a concentration below that of the nucleation. Here, we study whether and how the accumulation of NLs alters a lipid bilayer's mechanical properties. In synthetic systems, we found that NLs proffer unusual bilayer stretching capacities, especially in the presence of negatively curved phospholipids. This impact becomes spectacular when a lipid droplet is contiguous with the bilayer and supplies it with NLs. The tested NLs markedly decrease the bilayer area expansion modulus, significantly increase lysis tension but had opposite effects on membrane bending rigidity. Our data unveil how NL molecules modify overall membrane mechanics, the alteration of which may be linked to pathologies or anticancer treatments targeting NLs.

Significance:

Unlike phospholipids, neutral lipids (NLs) are non-surfactants, apolar fat, or oil molecules. They are synthesized in the endoplasmic reticulum (ER) bilayer and diffuse within the bilayer's hydrophobic region. At a critical concentration, the NLs phase separate within the bilayer to form an organelle called a lipid droplet (LD). However, even if they condense into LDs, a fraction of NLs remains in the bilayer. Also, under diverse pathological conditions associated with alterations in the ER structure or composition, NLs accumulate in the membrane, failing to condense efficiently into LDs. Their removal is crucial to preserve the multiple ER bilayer functions that rely on membrane mechanics. Here, we are interested in understanding how the presence of NLs impacts such mechanics.

Introduction

Organisms from protists to humans store excess energy in carbon-rich molecules that are often neutral lipids (NLs) (1, 2). NLs are apolar fat molecules, different from phospholipids, which are the building blocks of cellular membranes. The most abundant NLs are triacylglycerols, which are structurally the closest NL to phospholipids, and sterol esters, which are the most relative to cholesterol, another membrane constituent (3). However, other NLs are found depending on cell type and metabolic condition, such as retinyl ester, phytyl esters, squalene, acylceramides, etc. (2, 4–7). Most of these NLs are synthesized in the bilayer of the endoplasmic reticulum (ER) (8, 9). Because of their hydrophobicity, NLs accumulate within the bilayer's hydrophobic region as dissolved, mobile hydrophobic inclusions(10). When their concentration reaches a critical value, NLs phase separate within the bilayer and nucleate an oil lens (11, 12), which grows and buds off to become an independent organelle called a lipid droplet (LD) (8). In the context of nucleation phenomena, the formation of an LD consists of packaging a large fraction of the NLs into a condensed phase, in equilibrium with a dilute NL phase in the bilayer (7, 11).

Avoiding the accumulation of NLs in the ER membrane ensures its proper functioning. NL accumulation could increase the bilayer's thickness, which would likely cause membrane stresses and affect the stability of transmembrane proteins. Indeed, such an accumulation may alter membrane structure, fluidity, lipid distribution, and stability, which can cause various forms of membrane stress. Most of these disturbances can explain the onset of diseases or cell death when NL molecules accumulate in the ER bilayer and are not properly removed and packaged into LDs.

The assembly of triacylglycerol LDs is facilitated by membrane curvature, composition, and specific proteins (10, 13–18) that decrease the critical nucleation concentration (10, 19–21). Accordingly, when the ER's curved structure is lost due to the dysfunction in the ER shaping proteins, triacylglycerols accumulate in the bilayer, unable to effectively condense into LDs (10, 18). These conditions are associated with several diseases, such as spastic paraplegia (22). Other factors such as the ER membrane phospholipid composition and surface tension can also regulate the concentration of the bilayer-dissolved NLs (14) and their propensity to condense into LDs (23). Likewise, the NL chemistry determines its tendency to remain in the bilayer or condense into an LD (10, 14). Squalene, an intermediate molecule in the synthesis of sterols, is an example of an NL that abnormally accumulates in membranes (6, 14, 24). Increasing the

proportion of squalene relative to triacylglycerols leads to the formation of larger LDs (14), probably because squalene increases the nucleation concentration (6, 24) and decreases the budding propensity of LDs (14). Interestingly, many anticancer and antifungal drugs target the squalene epoxidase (25–27), leading to reduced cellular cholesterol and, inevitably, an accumulation of squalene. These two consequences may concomitantly contribute to cellular death.

In this paper, we ask the fundamental question of how NL molecules, referred to as fat or oil molecules hereafter, modulate the mechanical properties of a phospholipid bilayer. To answer this question, we used model membranes based on the formation of giant unilamellar vesicles (GUVs) containing neutral lipids, such as those from droplet-embedded vesicles (28, 29) or inverted emulsion vesicles (30). We found that oil molecules' presence substantially modifies the bilayer response to stretching and bending, depending on the phospholipid composition and oil type.

Results

Oil droplets expand the critical bilayer area strain while decreasing permeability.

We opted for osmotic swelling as a straightforward means to probe the expansion capacity of a giant unilamellar vesicle (GUV) bilayer (31–34) (**Figure 1A, top**). To investigate if NLs alter this expansion, we used the droplet-embedded vesicle system (DEV) (35), consisting of a giant unilamellar vesicle (GUV) containing an oil droplet made of triolein, the major triacylglycerol NL (**Figure 1A, bottom**). In the DEV system, the oil droplet equilibrates within seconds with a constant fraction of triolein molecules mobile in the bilayer (**Figure S1A-E**)(10).

We prepared GUVs and triolein oil-based DEVs (**Figure 1B**, **bottom**), both made of DOPC phospholipid, and we subjected them to the same osmotic shock. Both systems showed swelling and bursting cycles during which their bilayer underwent stretching and relaxation phases (31) (**Figure 1A-B**). To describe and understand the systems' response, we focused on the bilayer surface area strain ε for both GUVs and DEVs (**Figure 1C**). For DEVs, the bilayer area is calculated at each time point by withdrawing the space occupied by the droplet from the area of the sphere fitting the bilayer (**Figure 1C, Figure S1F-I**). Furthermore, the DEVs' swelling time took a few minutes (**Figure 1C,D**), much longer than the time it takes for triolein oil molecules to partition between the droplet and the bilayer (10). Therefore, the swelling process of DEVs occurred at equilibrium.

Triolein-DEVs had a slower strain rate than GUVs (initial slope, **Figure 1D**), which underwent many cycles within the same time-lapse. The strain rate is determined by the water flux, i.e., the permeability of the bilayer: the higher the permeability, the higher the strain rate. Accordingly, we found a permeability higher for GUVs, $24.8 \pm 8.3 \mu m.s^{-1}$, than triolein-DEVs, $9.0 \pm 2.6 \mu m.s^{-1}$ (**Figure 1E left, Figure S1J-M, supplemental text**) (36). Squalene-DEVs were less permeable than triolein-DEVs (**Figure 1E left, Figure S1J,L,M, supplementary text**), consistent with permeability studies with droplet interface bilayers (37).

The critical strain ε_{max}, reached when the bilayer bursts, was higher for DEVs than GUVs (**Figure 1D**, **Figure 1E right, Figure S1J).** A burst occurs when a critical pore size appears in the membrane. GUVs stretched at a slower strain rate have a higher probability of reaching the critical pore size (31) and, therefore, a lower ε_{max}. This correlation is not verified with DEVs, which had slower strain rates than GUVs while higher ε_{max} (**Figure 1D, Figure 1E right**). Therefore, other factors absent in GUVs favor the increase in ε_{max} for DEVs. We hypothesized

that oil molecules recruited to the bilayer are responsible for this higher critical bilayer strain for DEVs.

To test our hypothesis, we decided to vary the phospholipid composition, which controls the bilayer's oil concentration (14). We worked with different phospholipid mixtures, including DOPE (PE), DOPA (PA), DPPC, or PufaPC (18:0, 20:4). For each condition, we determined the critical bilayer strain, ε_{max}, and compared it between GUVs and DEVs (**Figure 1F, Figure S1N-R**). Irrespective of composition, triolein-DEV bilayers withstood larger expansions than GUVs (**Figure 1F, Figure S1R**). Interestingly, the critical bilayer strain of triolein-DEVs was systematically higher in the presence of negatively curved lipids such as PA and PE, between 3 and 5 times higher than for GUVs (**Figure 1F, Figure S1R**). We found that squalene enabled a higher membrane expansion than triolein in PC conditions and, more strikingly, in PufaPC (**Figure 1F, Figure S1R**). This particular increase in PufaPC may pertain to π-π interactions between the numerous unsaturations in the squalene's carbon skeleton and those in the PufaPC acyl chain. However, compositions containing PA and PE showed no difference between the two oils (**Figure 1F, Figure S1R**), suggesting that these phospholipids' contribution masked the difference between the two oils.

Stretching increases the bilayer oil concentration depending on the phospholipid composition.

Based on the above results, we hypothesize that the oil droplet buffers oil molecules to the bilayer, which has more material to withstand more significant expansions. Following this hypothesis, PA and PE would lead to more oil molecules in the bilayer.

To test our model, we used a fluorescently-labeled "triolein", triolein-NBD, mixed with triolein at 0.05% (w/w) to report for triolein localization (**Figure 2A**). The resulting DEV was then monitored during the osmotic swelling (**Figure 2B, left**). We found that the bilayer's triolein signal increased concomitantly with the bilayer stretching (**Figure 2B, right**). Then, the bilayer concentration sharply decreased following a rapid burst of the DEV (**Figure 2B, right**); the oil molecules almost spontaneously re-equilibrated between the droplet and the bilayer after this burst (**Figure 2B, Figure S2A**). These results show that increasing the bilayer surface tension by osmotic swelling raises the amount of oil in the bilayer, agreeing with previous *in silico* results (14) and confirmed here by using micropipettes to vary surface tension (**Figure S2B,C**). To test if squalene behaves like triolein, we used Bodipy, which labels the bilayer's

hydrophobicity, as we could not find available fluorescent squalene reporters. We observed a stronger Bodipy signal in the bilayer during osmotic swelling, most likely due to an increase in squalene in the bilayer (**Figure S2D**).

Our hypothesis suggests that the number of oil molecules incorporated into the bilayer during swelling determines the extent of membrane expansion. Since the critical bilayer strain depended on the phospholipid type (**Figure 1F, Figure S1R**), we measured the triolein increase in the bilayer for each phospholipid condition. We found an increase in the triolein signal during swelling for all lipid compositions but to different extents (**Figure 2D, Figure S2E**). We defined the bilayer triolein enrichment as the ratio between the triolein level in the bilayer at the maximum expansion (high tension) and the initially unstretched bilayer (low tension) (**Figure 2C**). We found that DEVs containing PA or PE, which had the most remarkable expansion (**Figure 1F**), displayed the highest triolein enrichment (**Figure 2D**). In contrast, triolein-DEVs made with PufaPC-PC, which did not significantly increase the critical bilayer strain (**Figure 1F**), exhibited a low triolein enrichment. These data are consistent with our model that, during stretching, triolein molecules can behave as membrane building blocks, like phospholipids, and allow for more bilayer expansion.

If our model is correct, then the enrichment level of triolein in the bilayer should dictate the critical bilayer strain. To test this prediction, we considered for each phospholipid composition the ratio of the critical bilayer strain of DEVs over GUVs (**Figure 1F**). This normalization cancels the contribution of phospholipids to the membrane expansion and highlights the contribution of triolein molecules. Consistent with our prediction, we found that the amount of triolein injected into the bilayer during stretching increases linearly with the critical bilayer strain ratio (**Figure 2E**).

In summary, an oil droplet connected to a bilayer equilibrates with residual oil molecules in the bilayer. The concentration of this residual oil increases as the bilayer is stretched. Phospholipids with negative spontaneous curvature favor a higher delivery of oil molecules from the droplet to the stretched bilayer and, thereupon, a higher critical bilayer strain.

The sole presence of oil molecules in a bilayer increases the critical area strain.

To fully demonstrate that the oil molecules favored the increase in the critical bilayer strain, we decided to repeat the previous experiments with oil molecules in the bilayer without any droplet

reservoir. To do so, we used the water-in-oil inverted emulsion method (30) by using a triolein oil phase containing triolein-NBD (**Figure 3A, left**). With this approach, indeed, we found that the resulting GUVs, called triolein-GUV (To-GUV), carried only triolein molecules in their bilayer (**Figure 3A, right**). The bilayer triolein concentration is defined as the triolein-NBD bilayer signal divided by Cy5-PE, reporting phospholipids (**Figure 3B**). Based on this normalization, triolein-GUVs and -DEVs composed of PC, and not subjected to an osmotic swelling, had a similar bilayer triolein signal (**Figure 3C**).

We first compared GUVs and triolein-GUVs, both made of PC, subjected to osmotic swelling. We found that the critical bilayer strain, ε_{max}, for triolein-GUVs was significantly higher than for GUVs (**Figures 3D**), consolidating our model that the sole presence of NLs is sufficient to increase the membrane expansion limit.

We next compared triolein-GUVs to triolein-DEVs. Triolein-DEVs had a 1.45 fold higher membrane expansion limit than triolein-GUVs in PC (**Figure 3D**). The presence of PA exacerbated this difference, by 3.2 fold higher (**Figure 3E, S3A-B**). These observations also agree with our model. Indeed, the bilayer of triolein-GUVs had a fixed number of oil molecules and, therefore, less material to withstand larger expansions; in contrast, the bilayer of triolein-DEV can be continuously supplied with oil molecules by the droplet. PA highlighted further this difference because it induced the most substantial triolein release into the bilayer of DEVs (**Figure 2D-E**). Finally, squalene had a similar impact than triolein in squalene-GUVs vs. squalene-DEVs (**Figure 3F**).

Overall, these data show that the oil molecules' presence increases the bilayer's ability to withstand more extensive stretching than a pure phospholipid membrane. If an NL droplet is physically connected to the bilayer, it will buffer NLs to the bilayer, further increasing its expansion. A dramatic consequence of such an increase in the bilayer stretching is that the area per phospholipid can be increased by several folds by NLs, especially in the presence of negatively curved phospholipids (**Figure 1F, Figure. 3D-F**).

Oil molecules modify the mechanical properties of a bilayer.

We wanted to know whether the mechanical properties of the bilayer are influenced by the presence of oil, as for solvents (38). The critical bilayer surface area strain is determined by the appearance of a critical pore size, which depends on membrane stretching and bending factors (31). We probed how NLs altered these mechanical factors independently.

First, we studied if NLs altered the lysis tension of DEVs, i.e., the surface tension at which a pore opens in the bilayer. We used micropipette suction to increase the surface tension of PC GUVs and PC DEVs made of triolein or squalene. The micropipette aspiration (MPA)-applied bilayer tension was increased continuously by pulling on the bilayer at a rate of approximately 2-3 mbar/sec (**Figure S4A**). The lysis tension was taken as the MPA-applied bilayer tension was recorded right before the bilayer's burst (**Figure S4A**). In PC, the lysis tension of GUVs was 8.1 ± 1.9 mN/m, in the range of previously reported values (36, 39). Triolein increased this lysis tension to 9.7 ± 1.9 mN/m, and squalene DEVs led to a more significant increase, to 10.8 ± 2.2 mN/m (**Figure 4A**). A similar trend was found for a PC/PA membrane composition (**Figure S4B**). This increase in the lysis tension can partly explain the higher critical bilayer area strain proffered by oil molecules (**Figure 1F, Figure S1R**).

Secondly, we determined the impact of the oil molecules on the area expansion modulus. For surface tensions over 0.5 mN/m, sufficient to smoothen thermal membrane fluctuations, the apparent area expansion modulus is given by Hooke's law (40, 41) (**Figure 4B**). Experimentally, we increased the bilayer area with a micropipette while recording its MPA-applied surface tension (**Figure 4B**). The slope of the resulting MPA-applied bilayer tension-area curve (**Figure S4C-D**) yields the apparent area expansion modulus of the bilayer (Y_{app}) (41). With this approach, we could only work with GUVs containing oils (**Figure 3A**) since, in DEVs, the droplet has a contribution in elasticity difficult to model. GUVs made of PC had an apparent expansion area modulus of 194 ± 25 mN/m (40), while those bearing triolein and squalene had lower values, 89 ± 31 mN/m and 111 ± 27 mN/m respectively (**Figure 4C**). This marked decrease in the apparent area expansion modulus is consistent with the overall increase in the critical bilayer strain observed when the NL oils are present in the bilayer **(Figure 3D-E**). However, no significant difference was found between squalene and triolein, suggesting that the apparent area expansion modulus does not solely account for the disparity in the bilayer expansion limit between these two oils (**Figure 1F**).

Finally, we determined the bending rigidity (K) by nanotube pulling experiments (**Figure 4D and S4E-I**). We found that the presence of triolein in a PC GUV bilayer decreased the bending rigidity (12 ± 4 k_BT) roughly by a factor of two compared to the value for a bare GUV (21 ± 4 k_BT) (**Figure 4E**); a similar trend was found when measuring the rigidity by fluctuation analysis

(42). Surprisingly, squalene slightly increased the bending rigidity (27 ± 4 k_BT), illustrating that oil molecules do not necessarily change membrane properties in the same way. We used the bending rigidity values to compute the absolute area expansion moduli (**Figure 4F**) (36). PC GUVs had an expansion area modulus of 214 ± 25 mN/m (40), while GUVs containing triolein or squalene had a lower value of 101 ± 35 mN/m and 120 ± 28 mN/m (**Figure 4F**).

In conclusion, the above data illustrate how and which membrane mechanical properties are altered by NL oil molecules. NLs can have similar or opposite effects on membrane mechanical properties, depending on the NLs' chemistry.

Discussion

Precise control of the biophysical properties of membranes is crucial for cell survival. Phospholipids and membrane proteins often control these properties. Here, we consider the impact of neutral lipids, which can behave as hydrophobic membrane inclusions. We found that neutral lipids proffer unusual mechanical properties to the bilayer membrane. Such an effect depends on the nature of the hydrophobic inclusion but also the phospholipid composition.

We worked with triolein, the main component of cellular LDs, and squalene, which can significantly accumulate in cells upon drug treatments targeting the squalene epoxidase (25–27). For the phospholipid conditions that we tested, we found that these neutral lipids increased the lysis tension of a bilayer and significantly decreased its area expansion modulus. While triolein decreased the bilayer bending stiffness, squalene increased it. Overall, these mechanical alterations are consistent with the greater membrane expansion proffered by the neutral lipids. At the molecular level, the increased critical membrane strain likely results from the insertion of neutral lipids between phospholipids when the membrane is stretched, i.e., when tension increases. Thus, the neutral lipids may adopt different molecular conformations when tension varies (43–45). At low tension, triolein molecules could remain perpendicular to the phospholipids but parallel to them at high tension, exposing their glycerol backbone to water (44). This molecular adaptability would allow phospholipids to be spaced further apart than in a pure bilayer.

Squalene is a long terpene with numerous unsaturation, chemically different from triolein. Despite contrasting chemistry, the two neutral lipids yielded similar elasticity. As for triolein, squalene may also adopt phospholipid-parallel or antiparallel orientations in the bilayer (46), depending on the surface tension, in a way that decreases the area expansion modulus. Concerning the membrane lysis tension, both neutral lipids increased it, especially squalene. This difference may pertain to the interaction spectrum of NLs with phospholipids. In particular, squalene can make multiple interactions π-π (47) with phospholipids, making it act like a molecular glue, “cross-linking” the bilayer leaflets and delaying the opening of a pore. Interestingly, squalene increased the bilayer bending rigidity, whereas triolein decreased it, relative to GUVs.

The bending rigidity (κ) depends on the bilayer thickness (d), the area expansion modulus (Y), and the coupling constant (β) of the monolayer leaflets composing the bilayer: $\kappa \propto \beta . d^2 . Y$ (48).

Triolein and squalene decreased by two, the area expansion modulus, Y, (**Figure 4F**), which tends to reduce the bending rigidity, but not for squalene (**Figure 4E**). Squalene particularly increases membrane thickness, more than triacylglycerols (37, 38, 49, 50). Also, via π-π interactions developed with phospholipids (47), squalene likely increases the monolayer coupling β. Consequently, the contribution of $\beta.d^2$ for squalene may compensate for the decrease in Y, sufficiently to overall increase the bending rigidity κ.

Based on the above analysis and the rigidity measurement (Figure 4E), curving squalene-rich membranes is more difficult. Squalene accumulation is promoted by several antifungal and anticancer drugs (25–27) and, therefore, the subsequent alteration in membrane mechanics could contribute to the death of fungal or cancer cells. Inducing the synthesis and membrane-accumulation of specific neutral lipids could be a strategy to prompt cancer cells to die.

Finally, our data show that a droplet connected to a bilayer can supply neutral lipids to the membrane, especially when the bilayer experiences stretching. The amount of neutral lipids delivered to the bilayer depends on the bilayer phospholipid composition. Thus, in a cellular context, LDs should be disconnected from the ER bilayer to avoid residual neutral lipids in the membrane. If not, the neutral lipid accumulation would hinder the ER 's multiple functions that rely on the precise regulation of its mechanical properties, involving membrane tubulation, stretching, budding, or fusion.

In conclusion, our study provides important insights into how neutral lipids can change membranes' biophysical properties. This study is relevant to better understand the ER membrane mechanics during fat storage, particularly in pathological conditions where neutral lipids fail to efficiently phase separate into LDs. Our approaches can be adapted to test the behavior of more exotic lipids.

ACKNOWLEDGMENTS

We are thankful to all the group members, Chloë Thimonier and Jean Goder, for their valuable comments and critical read of the manuscript. This work was supported the ANR-NANODROP, ANR-17-CE11-0003, ANR-MOBIL, ANR-18-CE11-0012-01 to ART.

Competing interests

The authors declare no competing interests.

Author contributions

ART designed research. AC and AS performed experiments and analyzed the data with LF. AC, AS, and ART wrote the manuscript.

1. Murphy, D.J., and J. Vance. 1999. Mechanisms of lipid-body formation. *Trends Biochem. Sci.* 24:109–115.

2. van Wijk, K.J., and F. Kessler. 2017. Plastoglobuli: plastid microcompartments with integrated functions in metabolism, plastid developmental transitions, and environmental adaptation. *Annu. Rev. Plant Biol.* 68:253–289.

3. Walther, T.C., and R.V. Farese. 2012. Lipid droplets and cellular lipid metabolism. *Annu. Rev. Biochem.* 81:687–714.

4. Ajat, M., M. Molenaar, J.F. Brouwers, A.B. Vaandrager, M. Houweling, and J.B. Helms. 2017. Hepatic stellate cells retain the capacity to synthesize retinyl esters and to store neutral lipids in small lipid droplets in the absence of LRAT. *Biochim. Biophys. Acta BBA-Mol. Cell Biol. Lipids*. 1862:176–187.

5. Senkal, C.E., M.F. Salama, A.J. Snider, J.J. Allopenna, N.A. Rana, A. Koller, Y.A. Hannun, and L.M. Obeid. 2017. Ceramide is metabolized to acylceramide and stored in lipid droplets. *Cell Metab.* 25:686–697.

6. Spanova, M., T. Czabany, G. Zellnig, E. Leitner, I. Hapala, and G. Daum. 2010. Effect of lipid particle biogenesis on the subcellular distribution of squalene in the yeast Saccharomyces cerevisiae. *J. Biol. Chem.* 285:6127–6133.

7. Thiam, A.R., and E. Ikonen. 2020. Lipid Droplet Nucleation. *Trends Cell Biol.*

8. Olzmann, J.A., and P. Carvalho. 2018. Dynamics and functions of lipid droplets. *Nat. Rev. Mol. Cell Biol.* 1.

9. Pol, A., S.P. Gross, and R.G. Parton. 2014. Review: biogenesis of the multifunctional lipid droplet: lipids, proteins, and sites. *J. Cell Biol.* 204:635–646.

10. Santinho, A., V.T. Salo, A. Chorlay, S. Li, X. Zhou, M. Omrane, E. Ikonen, and A.R. Thiam. 2020. Membrane Curvature Catalyzes Lipid Droplet Assembly. *Curr. Biol.* 30:2481-2494.e6.

11. Thiam, A.R., and L. Forêt. 2016. The physics of lipid droplet nucleation, growth and budding. *Biochim. Biophys. Acta*. 1861:715–722.

12. Khandelia, H., L. Duelund, K.I. Pakkanen, and J.H. Ipsen. 2010. Triglyceride blisters in lipid bilayers: implications for lipid droplet biogenesis and the mobile lipid signal in cancer cell membranes. *PloS One*. 5:e12811.

13. Adeyo, O., P.J. Horn, S. Lee, D.D. Binns, A. Chandrahas, K.D. Chapman, and J.M. Goodman. 2011. The yeast lipin orthologue Pah1p is important for biogenesis of lipid droplets. *J. Cell Biol.* 192:1043–1055.

14. Ben M'barek, K., D. Ajjaji, A. Chorlay, S. Vanni, L. Forêt, and A.R. Thiam. 2017. ER Membrane Phospholipids and Surface Tension Control Cellular Lipid Droplet Formation. *Dev. Cell*. 41:591-604.e7.

15. Choudhary, V., O. El Atab, G. Mizzon, W.A. Prinz, and R. Schneiter. 2020. Seipin and Nem1 establish discrete ER subdomains to initiate yeast lipid droplet biogenesis. *J. Cell Biol.* 219.

16. Joshi, A.S., B. Nebenfuehr, V. Choudhary, P. Satpute-Krishnan, T.P. Levine, A. Golden, and W.A. Prinz. 2018. Lipid droplet and peroxisome biogenesis occur at the same ER subdomains. *Nat. Commun.* 9:2940.

17. Kassan, A., A. Herms, A. Fernández-Vidal, M. Bosch, N.L. Schieber, B.J. Reddy, A. Fajardo, M. Gelabert-Baldrich, F. Tebar, and C. Enrich. 2013. Acyl-CoA synthetase 3 promotes lipid droplet biogenesis in ER microdomains. *J Cell Biol*. 203:985–1001.

18. Wang, S., F.-Z. Idrissi, M. Hermansson, A. Grippa, C.S. Ejsing, and P. Carvalho. 2018. Seipin and the membrane-shaping protein Pex30 cooperate in organelle budding from the endoplasmic reticulum. *Nat. Commun.* 9:2939.

19. Chung, J., X. Wu, T.J. Lambert, Z.W. Lai, T.C. Walther, and R.V. Farese Jr. 2019. LDAF1 and Seipin Form a Lipid Droplet Assembly Complex. *Dev. Cell*.

20. Zoni, V., W. Shinoda, and S. Vanni. 2020. Seipin accumulates and traps diacylglycerols and triglycerides in its ring-like structure. *bioRxiv*.

21. Prasanna, X., V.T. Salo, S. Li, K. Ven, H. Vihinen, E. Jokitalo, I. Vattulainen, and E. Ikonen. 2020. Seipin traps triacylglycerols to facilitate their nanoscale clustering in the ER membrane. *bioRxiv*. 2020.10.26.355065.

22. Renvoisé, B., B. Malone, M. Falgairolle, J. Munasinghe, J. Stadler, C. Sibilla, S.H. Park, and C. Blackstone. 2016. Reep1 null mice reveal a converging role for hereditary spastic paraplegia proteins in lipid droplet regulation. *Hum. Mol. Genet.* 25:5111–5125.

23. Zoni, V., R. Khaddaj, P. Campomanes, R. Thiam, R. Schneiter, and S. Vanni. 2020. Lipid droplet biogenesis is driven by liquid-liquid phase separation. *Dev.-CELL--20-00075*.

24. Spanova, M., D. Zweytick, K. Lohner, L. Klug, E. Leitner, A. Hermetter, and G. Daum. 2012. Influence of squalene on lipid particle/droplet and membrane organization in the yeast Saccharomyces cerevisiae. *Biochim. Biophys. Acta BBA-Mol. Cell Biol. Lipids*. 1821:647–653.

25. Petranyi, G., N.S. Ryder, and A. Stutz. 1984. Allylamine derivatives: new class of synthetic antifungal agents inhibiting fungal squalene epoxidase. *Science*. 224:1239–1241.

26. Brown, A.J., N.K. Chua, and N. Yan. 2019. The shape of human squalene epoxidase expands the arsenal against cancer. *Nat. Commun.* 10:1–4.

27. Cirmena, G., P. Franceschelli, E. Isnaldi, L. Ferrando, M. De Mariano, A. Ballestrero, and G. Zoppoli. 2018. Squalene epoxidase as a promising metabolic target in cancer treatment. *Cancer Lett.* 425:13–20.

28. Chorlay, A., and A.R. Thiam. 2018. An asymmetry in monolayer tension regulates lipid droplet budding direction. *Biophys. J.* 114:631–640.

29. Chorlay, A., L. Monticelli, J.V. Ferreira, K.B. M'barek, D. Ajjaji, S. Wang, E. Johnson, R. Beck, M. Omrane, and M. Beller. 2019. Membrane Asymmetry Imposes Directionality on Lipid Droplet Emergence from the ER. *Dev. Cell*.

30. Pautot, S., B.J. Frisken, and D.A. Weitz. 2003. Production of unilamellar vesicles using an inverted emulsion. *Langmuir*. 19:2870–2879.

31. Chabanon, M., J.C. Ho, B. Liedberg, A.N. Parikh, and P. Rangamani. 2017. Pulsatile lipid vesicles under osmotic stress. *Biophys. J.* 112:1682–1691.

32. Oglęcka, K., P. Rangamani, B. Liedberg, R.S. Kraut, and A.N. Parikh. 2014. Oscillatory phase separation in giant lipid vesicles induced by transmembrane osmotic differentials. *Elife*. 3:e03695.

33. Sandre, O., L. Moreaux, and F. Brochard-Wyart. 1999. Dynamics of transient pores in stretched vesicles. *Proc. Natl. Acad. Sci.* 96:10591–10596.

34. Karatekin, E., O. Sandre, H. Guitouni, N. Borghi, P.-H. Puech, and F. Brochard-Wyart. 2003. Cascades of transient pores in giant vesicles: line tension and transport. *Biophys. J.* 84:1734–1749.

35. Chorlay, A., A. Santinho, and A.R. Thiam. 2020. Making Droplet-Embedded Vesicles to Model Cellular Lipid Droplets. *STAR Protoc.* 100116.

36. Olbrich, K., W. Rawicz, D. Needham, and E. Evans. 2000. Water permeability and mechanical strength of polyunsaturated lipid bilayers. *Biophys. J.* 79:321–327.

37. Faugeras, V., O. Duclos, D. Bazile, and A.R. Thiam. 2020. Membrane determinants for the passive translocation of analytes through droplet interface bilayers. *Soft Matter*. 16:5970–5980.

38. Needham, D., and D.A. Haydon. 1983. Tensions and free energies of formation of" solventless" lipid bilayers. Measurement of high contact angles. *Biophys. J.* 41:251–257.

39. Evans, E., V. Heinrich, F. Ludwig, and W. Rawicz. 2003. Dynamic tension spectroscopy and strength of biomembranes. *Biophys. J.* 85:2342–2350.

40. Kwok, R., and E. Evans. 1981. Thermoelasticity of large lecithin bilayer vesicles. *Biophys. J.* 35:637–652.

41. Rawicz, W., K.C. Olbrich, T. McIntosh, D. Needham, and E. Evans. 2000. Effect of chain length and unsaturation on elasticity of lipid bilayers. *Biophys. J.* 79:328–339.

42. Pakkanen, K.I., L. Duelund, K. Qvortrup, J.S. Pedersen, and J.H. Ipsen. 2011. Mechanics and dynamics of triglyceride-phospholipid model membranes: Implications for cellular properties and function. *Biochim. Biophys. Acta BBA-Biomembr.* 1808:1947–1956.

43. Hamilton, J.A. 1989. Interactions of triglycerides with phospholipids: incorporation into the bilayer structure and formation of emulsions. *Biochemistry*. 28:2514–2520.

44. Pakkanen, K.I., L. Duelund, M. Vuento, and J.H. Ipsen. 2010. Phase coexistence in a triolein–phosphatidylcholine system. Implications for lysosomal membrane properties. *Chem. Phys. Lipids*. 163:218–227.

45. Bacle, A., R. Gautier, C.L. Jackson, P.F. Fuchs, and S. Vanni. 2017. Interdigitation between triglycerides and lipids modulates surface properties of lipid droplets. *Biophys. J.* 112:1417–1430.

46. Tarun, O.B., M.Y. Eremchev, and S. Roke. 2018. Interaction of oil and lipids in freestanding lipid bilayer membranes studied with label-free high-throughput wide-field second-harmonic microscopy. *Langmuir*. 34:11305–11310.

480 47. Hildebrandt, E., A. Dessy, J.-H. Sommerling, G. Guthausen, H. Nirschl, and G. Leneweit.
481 2016. Interactions between phospholipids and organic phases: insights into lipoproteins
482 and nanoemulsions. *Langmuir*. 32:5821–5829.

483 48. Bermudez, H., D.A. Hammer, and D.E. Discher. 2004. Effect of bilayer thickness on
484 membrane bending rigidity. *Langmuir*. 20:540–543.

485 49. Gross, L.C., A.J. Heron, S.C. Baca, and M.I. Wallace. 2011. Determining membrane
486 capacitance by dynamic control of droplet interface bilayer area. *Langmuir*. 27:14335–
487 14342.

488 50. Waldbillig, R.C., and G. Szabo. 1979. Planar bilayer membranes from pure lipids.
489 *Biochim. Biophys. Acta BBA-Biomembr.* 557:295–305.

490 51. Hochmuth, R.M., and E.A. Evans. 1982. Extensional flow of erythrocyte membrane from
491 cell body to elastic tether. I. Analysis. *Biophys. J.* 39:71–81.

492

493

494

495

Figure 1: Oil droplets connected to a bilayer expand the critical membrane area strain.
A) Top: Schematic representation of the behavior of a GUV under hypotonic shock. GUVs undergo swelling and burst cycles. **Bottom**: Schematic representation of a triolein DEV (Droplet Embedded Vesicle) system compared to a GUV which also undergo swelling and burst cycles**. B)** Time-lapse of triolein DEV and GUV during a hypotonic shock experiment. Black dashed circles report maximum vesicle radius. Scale bar is 10µm. **C) Top:** Green arc underlying the bilayer area for an uninflated and inflated DEV. **Bottom:** Formula used to compute the bilayer strain, ε, defined as the relative expansion of the bilayer area. **D)** Corresponding bilayer strain ε variations of triolein DEV and GUV over time of Figure 1B. Swelling and burst cycles are clearly visible for GUVs (blue points; 6 cycles) and DEVs (green points; 1 cycle). **E) Left:** Plot of the initial water permeability of PC bilayer of GUVs (n=8), triolein-DEVs (n=9) and squalene-DEVs (n=9). Mean +/- SD. **Right:** Plot of the critical bilayer strain (ε_{max}) of GUVs (blue, n=28), triolein-DEVs (green, n=29) and squalene-DEVs (grey, n=21) for PC bilayer. Mean +/- SD. **F)** Plot of the critical bilayer strain (ε_{max}) of GUVs (blue), triolein-DEVs (green) and squalene-DEVs (grey) for various phospholipid compositions of the bilayer. Mean +/- SD.

Figure 2: Stretching increases the oil concentration in the bilayer depending on the phospholipid composition.
A) Schematic representation of the triolein DEV formation protocol. To report triolein distribution, triolein was supplemented with 0,05% (w/w) triolein-NBD. **B) Left**, confocal images of PC triolein DEVs under hypotonic shock with triolein tagged by triolein-NBD. Line scans show a triolein-NBD signal colocalizing with the bilayer. Scale bar is 5µm.**Right**, corresponding quantification of triolein-NBD signal and bilayer area variation. During bilayer stretching, triolein-NBD signal increased, and quickly dropped after deflation. **C)** Representative confocal fluorescence images of a PC triolein-DEVs at the maximum bilayer expansion state (high tension) and at the "unstretched" state (low tension). Linescans allow for quantification of triolein-NBD fluorescence intensity in the bilayer in each state. 'Triolein enrichment' was computed by taking the fluorescence ratio between stretched state and unstretched state. Scale bar is 5 µm. **D)** Triolein enrichment measured for PC (n=8), PA-PC (n=5), PE-PC (n=4), DPPC-PC (n=3) and PufaPC-PC (n=8) triolein-DEVs. Mean +/- SD. **E)** Plot of the critical bilayer strain ratio between DEV and GUV against the triolein enrichment for previous phospholipid compositions. Statistical analysis revealed a significant slope different from zero for a linear fit (dotted lines). Mean +/- SD.

Figure 3: The sole presence of oil molecules increases the critical bilayer strain.
A) Left, illustration of the formation of triolein-GUVs (To-GUVs) using a water-in-oil inverted emulsion method. The triolein was tagged with 0,05% (w/w) of triolein-NBD. **Right**, fluorescence confocal imaging of the resulting triolein-GUVs. Significant triolein-NBD signal colocalize with the bilayer reported by Cy5-PE. Scale bar: 5µm. **B) Top:** three different model systems: a bilayer with no

neutral lipids (GUV) , a bilayer supplemented with triolein molecules (To-GUV) and a bilayer supplemented with triolein molecules provide by a triolein droplet (To-DEV). **Bottom:** to assess the concentration of triolein in the bilayer of the three model systems, we compute the 'triolein in bilayer' by taking the fluorescence ratio between triolein-NBD signal and Cy5-PE signal; microscope settings were kept constant. **C)** Quantification of the triolein in bilayer for GUVs (n=6), triolein-GUVs (n=13) and triolein-DEVs (n=49) made with PC phospholipids. Mean +/- SD. T-test show no significant difference of triolein in bilayer between triolein-GUVs and triolein-DEVs. **D)** Quantification of the critical bilayer strain ($\boldsymbol{\varepsilon}_{max}$) of PC GUVs (n=28), triolein-GUVs (n=41) and triolein-DEVs (n=29), showing higher stretching for DEVs and GUVs containing oil. Mean +/- SD. **E)** Plot of the critical bilayer strain ($\boldsymbol{\varepsilon}_{max}$) for PC-PA GUVs (n=9), triolein-GUVs (n=15) and triolein-DEVs (n=6) showing higher stretching for DEVs and GUVs containing oil. Mean +/- SD. **F)** Quantification of the critical bilayer strain ($\boldsymbol{\varepsilon}_{max}$) of PC GUVs (n=28), squalene-GUVs (Sq-GUV) (n=7) and squalene-DEVs (Sq-DEVs) (n=21), showing higher stretching for DEVs and GUVs containing oil. Mean +/- SD.

Figure 4: Oil molecules modify the mechanical properties of a bilayer.

A) Bilayer lysis tension measured for GUVs (n=43), triolein-DEVs (n=24) and squalene-DEVs (n=41), made with PC. Mean +/- SD. **B)** Illustration of the experimental setup to determine the apparent area expansion modulus of a bilayer. Thanks to micropipettes, tension is measured while increasing the bilayer area. Apparent area expansion modulus (Y) is computed from the ratio between surface tension and area variation. **C)** Apparent area expansion modulus of PC GUVs (n=5), triolein-GUVs (n=7) and squalene-GUVs (n=5). Mean +/- SD. The presence of neutral lipids in the bilayer (triolein or squalene) decreases apparent area expansion modulus. see also (**Figure S4 C-E). D)** Experimental determination of the bending modulus (K) by pulling a nanotube from the bilayer. The bending modulus is directly linked to the nanotube radius and the membrane tension. For further details see (**Figure S4E-I**). **E)** Bending modulus of GUVs (n=7), triolein-GUVs (n=4) and squalene-GUVs (n=3) made with PC. Mean +/- SD. The presence of triolein in the bilayer results in a significant bending modulus decrease. Squalene increases the bending modulus. **E)** Area expansion modulus of PC GUVs (n=5), triolein-GUVs (n=7) and squalene-GUVs (n=5). Mean +/- SD. The presence of neutral lipids in the bilayer (triolein or squalene) decreases area expansion modulus.

MATERIALS AND METHODS

All experiments were performed in the following HKM buffer: 50 mM Hepes, 120 mM K-acetate, and 1 mM MgCl2 (in Milli-Q water) at pH 7.4 and 280±15 mOsm.

Preparation of GUVs.

GUVs were prepared by electro-formation. Phospholipids and mixtures thereof in chloroform at 0.5µM were dried on an indium tin oxide (ITO) coated glass plate. The lipid film was desiccated for 1 h. The chamber was sealed with another ITO coated glass plate. The lipids were then rehydrated with a sucrose solution (280+-15 mOsm). Electro-formation is performed using 100 Hz AC voltage at 1.0 to 1.4 Vpp and maintained for at least 2h. This low voltage was used to avoid hydrolysis of water and dissolution of the titanium ions on the glass plate. GUVs were either stored in the chamber at 4°C overnight or directly collected with a Pasteur pipette.

GUVs composition for used Phospholipids mixtures:

PC GUVs were 100 % PC, PE-PC GUVs were 50% PE and 50% PC, PA-PC GUVs were 30% PA and 70% PC, DPPC-PC GUVs were 40% DPPC and 60% PC, PufaPC-PC GUVs were 30% PufaPC and 70% PC.

Preparation of DEVs

To prepare the oil droplets, 5 µL of the oil (triolein or squalene) was added to 70 µL of HKM buffer. The mixture was sonicated. The diameter of the resulting droplets is on the order of a few hundred nanometers. To make DEV, GUVs were then incubated with the LDs for 5 min. To make DEV with triolein-NBD, the oil was composed of 99,95% of triolein and 0,05% (w/w) of To-NBD. The GUV-LD mixture was then placed on a glass coverslip (pretreated with 10 % (w/w) BSA and washed three times with buffer) and observed with a confocal microscope.

Preparation of GUVs by the inverted emulsion technique

Two phospholipids mixtures were diluted in chloroform at 0.5 µM and dried. A 150µL oil volume was poured onto one mixture and 200µL of HKM-buffer onto the other one. These solutions were sonicated for 5 minutes to facilitates the solubilization of phospholipids. A 100µL volume of the oil-phospholipid mixture was deposited on the HKM-phospholipids solution. Then, the remaining 50µL of the oil-phospholipid mixture was mixed with 4µL of an HKM-sucrose 1:1 (w/w) solution to generate a water-in-oil inverted micro-emulsion which was

then added to the HKM-contacting-oil solution. The resulting mixture was centrifuged for three minutes. The oil-containing GUVs were next collected in the aqueous volume.

Confocal microscope images

All micrographs of DEV were made on a Carl ZEISS LSM 800 with an X63 oil immersion objective or X10 air objective, and observed samples were held by Glass coverslips (Menzel Glaser (24x36mm #0)).

Hypotonic shock

DEVs were produced following the techniques described above. The resulting solution was placed on a coverslip (pretreated with 10 % (w/w) BSA and washed three times with buffer) and observed with a confocal microscope (x10 objective). Spherical DEVs with no thermal fluctuation of the bilayer have been selected so that the surface of the bilayer can be easily determined. Next, 50µL of MQ water was added to 120µL of DEV solution to applied an osmotic shock of ΔC=80mOsm. The osmotic gradients applied were always the same (ΔC=80mOsm for **Figure 1,2,3 and Figure S1,S2,S3**) except for (**Figure 1D,E and Figure S1J-M** due to permeability protocol precautions) where the ΔC was 145mOsm and for (**Figure 2B and Figure S2A** to report rapid triolein partitioning) where ΔC was 210mOsm. The DEVs were then imaged overtime to follow the evolution during swelling. The same protocol was used to apply hypotonic shock to GUVs or Oil-containing-GUVs (**Figure 1F, 2D, 3D,E,F**).

Determination of the critical bilayer strain ε_{max}

The maximum expansion of the bilayer is given by the following equation:

$$\epsilon_{max} = \frac{A_{max} - A_0}{A_0}$$

where A_{max} and A_0 are respectively the maximal areas of the bilayer before burst (stretched state) and the area before starting the swelling experiments (unstretched state). This area was determined by fitting a circle onto the DEV (GUV) bilayer and recording its radius. The radius of the embedded droplets was also recorded for DEV swelling experiments to determine the corrected surface area of the DEVs bilayer (see the section below).

Bilayer surface area of the DEVs

To consider only the surface of the DEV's bilayer, the surface occupied by the embedded droplet had to be removed. To do this, we calculated the surface of the sphere formed by the

bilayer and subtracted the surface of the spherical cap corresponding to the droplet (Figure S1C). This gave the following expression of the surface area of the DEV bilayer (A)

$$A_{DEV} = 2\pi R_g^2.(1 + \sqrt{1 - (\frac{R_d}{R_g})^2})$$

where R_g and R_d are respectively the DEV radius and droplet radius.

Permeability assay

To determine permeability, we made osmotic shock experiments thanks to an applied osmotic gradient between the outside and inside of the vesicles of ΔC=145mOsm. To do so, we added 20µL of DEVs (or GUVs) sucrose solution (280±15 mOsm) into 100µL HKM buffer. Then, we added 100µL of Milli-Q water to induce an osmotic shock. During the experiment, we maintained the DEVs (or the GUVs) thanks micropipettes, to have a clear determination of both vesicle radius and droplet radius (**See Figure 1C, and supplemental material 1**). This enables to determine the permeation area and the volume of the vesicle as a function of time during the swelling experiment.

GUVs, triolein-DEV,s and squalene-DEVs initial permeability computation

See supplemental material 1 for the computation of the initial permeability.

Determination of the triolein concentration in the bilayer and following of this concentration as a function of time

To determine the concentration of triolein molecules in the bilayer, we used triolein-DEV (triolein GUVs). The triolein mixture was made of 99,95% triolein and 0,05% (w/w) of triolein-NBD. For all our experimental conditions involving these measurements (**Figures 1,2 and 3**), we chose DEVs (triolein GUVs) which radius was between 5 and 15 microns with micrometric triolein droplets. DEVs snap were taken by keeping the same settings for each DEVs. Then, fluorescence profiles were drawn perpendicular to the bilayer of triolein-DEVs (triolein GUVs) and averaged over 15 pixels. The maximum value of the profiles was recorded and averaged over multiple DEVs. The same protocol was used for Cy5-PE fluorescence signals measurements (**Figure 3C**). For monitoring of triolein concentration in the bilayer (**Figure S1D-E**), we captured images every 5 minutes to avoid bleaching of the triolein-NBD signal.

FRAP experiment, triolein-NBD bleaching in the Bilayer

FRAP experiments were performed by bleaching a part of the DEV bilayer (**Figure S1B-C**). To-NBD signal was bleached, then, the fluorescence signal recovery was monitored. The FRAP curve is normalized by the fluorescence before bleaching DEVs and just after the bleach (in non-bleached regions). GraphPad Prism was used to fit the FRAP recovery curve with a non-linear regression and the exponential "one-phase association model".

Bodipy fluorescence in squalene DEVs during hypotonic shock

To follow bodipy fluorescence signal during hypotonic shock upon squalene DEVs (**Figure S2F**), 0,5µL of bodipy was added in 100µL of HKM buffer containing Squalene DEVs. After 10 minutes, 20µL of water was added to the coverslip and the evolution of bodipy signal in the bilayer of the Squalene DEV was monitored.

Micromanipulation & surface tension measurements by micropipette aspiration applied bilayer tension (MPA-applied bilayer tension).

Micropipettes were made from capillaries drawn out with a Sutter Instruments pipette puller. They were used to manipulate GUVs, DEVs, or GUVs containing oil. The pipettes were incubated for 30 min in a 5% BSA solution before use, to prevent droplets and membranes from adhering to the glass.

Additionally, surface tensions of bilayers were measured using the same pipettes. Using Laplace's law, and measuring the pipette inner radius, the GUV radius, and suction pressure, the surface tension of the bilayer can be determined by:

$$\gamma = \frac{\Delta P_{suc}}{2\left(\frac{1}{R_p} - \frac{1}{R_g}\right)}$$

where ΔP_{suc}, R_p, and R_g are the suction pressure, the pipette inner radius, and the vesicle radius, respectively

The suction was carried out using a syringe. The resulting pressure was measured with a pressure transducer (DP103 provided by Validyne Eng. Corp, USA), the output voltage of which was monitored with a digital voltmeter. The pressure transducer (range 55 kPa) was calibrated before the experiments. Micro-pipettes made from capillaries (1.0oDx0.58iDx150Lmm 30-0017 GC100-15b Harvard Apparatus) with a micropipette puller (Sutter instrument model P-2000). Micromanipulation (Eppendorf TransferMan! 4r). Pressure measurement unit (DP103 provided by Validyne eng. corp, USA).

For bending rigidity measurements (see below, **Bending rigidity measurements)**, that needed a better measurement precision, the suction was applied thanks to a water reservoir whose height was control with a micrometer gauge (precision 0.005 mm). The resulting suction pressure was determined thanks to the measurement of the water level variation.

Lysis tension measurements

To determine an estimation of the bilayer lysis tension of GUVs, DEVs, or GUVs containing oil, we used the micropipette aspiration technique. Thanks to a slight aspiration, a bilayer tongue was sucked in the micropipette. The aspiration was then increased at an approximate rate of 2-3 mbar/sec, causing a proportional increase in the bilayer surface tension (see above, **Micromanipulation & surface tension measurements)**. At a certain tension, the bilayer ruptured because of a pore opening. The measured lysis tension was taken as the higher tension reached just before bilayer rupture.

Bending rigidity measurements

First, nanotubes were pulled from GUVs or oil-GUVs: Streptavidin-coated microspheres were added to the bulk on the glass coverslip. Then, the GUV was gently captured by one of the two micro-pipettes to control surface tension γ. One streptavidin-coated microsphere was caught by the other micro-pipette and it was slowly moved toward the GUV. Upon contact, the biotinylated phospholipid of the GUV interacted strongly with the streptavidin-coated microsphere surface. Finally, a nanotube was pulled by removing slowly the micropipette in the opposite direction to the GUV.

The bending rigidity was obtained with the following equation:

$$R_t = \sqrt{\frac{\kappa}{2\gamma}}$$

Where κ is the bending rigidity of the membrane which has to be determined with the experimental measurements of the bilayer tension γ (see **Micromanipulation & surface tension measurements by micro-aspiration** section) and nanotube radius R_t.

To obtain R_t, we vary the tube length at a constant displacement velocity of 2,5µm.s^{-1} at constant surface tension, which keeps the radius constant based on the previous equation.

Therefore, for a given tension, we have many couples of tube length L_t and tongue length L_p in the micropipette. The conservation of surface yields:

$$L_p = \delta . L_t + b$$

Thus, from this conservation, the slope (δ) was extracted by measuring different couples of L_p and L_t. We also checked that we do not detect hysteresis on these curves (**Figure S4H-I**) to ensure that we reached equilibrium for the oil partitioning (for triolein-GUV and squalene-GUV) between the nanotube and the GUV.

On the other hand, conservation of the volume of the system links the radius of the tube to that of the GUV (Rg) and the pipette through the following equation (51):

$$R_t = \delta . \left(1 - \frac{R_p}{R_g}\right) . R_p$$

Finally, different values of R_t, associated with a different value of γ were measured, gave us a mean value for κ with the first equation of this section.

Apparent area expansion modulus measurements

GUVs or Oil-containing-GUVs were gently captured with a micropipette. Then, aspiration in the micropipette was slowly increased to obtain multiple values of membrane tension (approximately 20 sec between each point). For each value of MPA-applied bilayer tension the variation of the length of the bilayer tongue in the micropipette and the radius of the GUV was measured allowing to determine an approximate variation at the first order of the surface area of the bilayer of the GUV ΔA (36) :

$$\Delta A = 2\pi R_p (1 - R_p/R_g) \Delta L_p$$

where ΔL_p, R_p, and R_g are respectively the variation of the bilayer tongue length in the micropipette, the pipette inner radius, and the GUV radius.

The MPA-applied bilayer tension was then plotted against the relative surface area variation of the GUV's bilayer. As the GUV was already slightly tensed (initial tension above 0.1 mN/m) the membrane fluctuation is negligible and the MPA-applied bilayer tension (γ) can be linked to the surface area variation ($\Delta A/A_0$) by the apparent area expansion modulus (Y):

$$Y_{app} = \frac{\gamma}{\Delta A/A_0}$$

Therefore, the slope of the MPA-applied bilayer tension -surface area variation curve gave the apparent area expansion modulus of the membrane (Y_{app}).

Area expansion modulus computing

Area expansion modulus was determined following the experiment in the "apparent area expansion modulus measurements" section and previously determined bending rigidity κ. To plot the MPA-applied bilayer tension γ against the relative surface area variation $\Delta A/A_0$ as above, the MPA-applied bilayer tension is the plot as a function of :

$$\frac{\Delta A}{A_0} + \Delta\alpha$$

With

$$\Delta\alpha = -(K_B T/8\pi\kappa)\ln(\gamma/\gamma_0)$$

K_B is the Boltzmann constant, T the room temperature in Kelvin and γ_0 the initial MPA-applied bilayer tension at the beginning of the experiment. Therefore, the slope of the MPA-applied bilayer tension - $\frac{\Delta A}{A_0} + \Delta\alpha$ curve gave the area expansion modulus (Y) (36).

QUANTIFICATION AND STATISTICAL ANALYSIS

Statistical analysis

The statistical comparison was made using student a parametric test where we assume a Gaussian distribution. Then the test is an unpaired t-test. The statistical analysis were made by GraphPad Prism 7.0a and "***" indicates $p < 0.0005$, "**" indicates $p < 0{,}005$ and "*" indicates $p < 0.05$.

When the bar graph is plotted, values shown in the text and figures are mean ± S.D. When only the data set of one experiment is shown, the values on the graph are absolute value ± uncertainty of measurements.

EQUIPMENT AND REAGENTS

Equipment

All micrographs were made on a Carl ZEISS LSM 800. Glass coverslips: Menzel Glaser (24x36mm #0). Micro-pipettes made from capillaries (1.0ODx0.58IDx150Lmm 30-0017 GC100-15b Harvard Apparatus) with a micropipette puller (Sutter instrument model P-2000). Micromanipulation (Eppendorf TransferMan® 4r). Pressure measurement unit (DP103 provided by Validyne eng. corp, USA).

Chemical products:

Phospholipids: PC (1,2-dioleyl-sn-3glycero-3-phosphocholine), PE (1,2-dioleoyl-sn-glycero-3-phosphoethanolamine), PA (1,2-dioleoyl-sn-glycero-3-phosphate), DPPC (1,2-dipalmitoyl-sn-glycero-3-phosphocholine), PufaPC 18:0-20:4 (1-stearoyl-2-arachidonoyl-sn-glycero-3-phosphocholine), biotynil-PE (1,2-dioleyl-sn-glycero-3-phosphoetanolamine-N-(biotinyl), Rh-PE (1,2-dioleyl-sn-glycero-3-phosphoethanolamine-N-lissamine rhodamine B sulfonyl) and Cy5-PE (1,2-dioleoyl-sn-glycero-3-phosphoethanolamine-N-(Cyanine 5)) were from Avanti Polar Lipids. Bodipy 493/503 was from Thermo Fisher Scientific. Triolein and squalene were from Sigma Aldrich and To-NBD (1,3-Di(cis-9-octadecenoyl-2-((6-(7-notrobenz-2-oxa-1, 3-diazol-4-yl) amino) hexanoyl) glycerol was from Setareh biotech. Streptavidin-coated microspheres were from Bangs Laboratories. Hepes (54457–250-F), K acetate (P1190), MgCl2 (M8266-100G), BSA 98% (A7906-100G), and sucrose 99.5% (59378-500G) were from Sigma-Aldrich.

Fat Inclusions Strongly Alter Membrane Mechanics.

Alexandre Santinho[1,§], Aymeric Chorlay[1,§], Lionel Foret[1], Abdou Rachid Thiam[1]*

[1] Laboratoire de Physique de l'École Normale Supérieure, ENS, Université PSL, CNRS, Sorbonne Université, Université de Paris, F-75005 Paris, France

[§] These authors contributed equally to this work

Supplemental figures

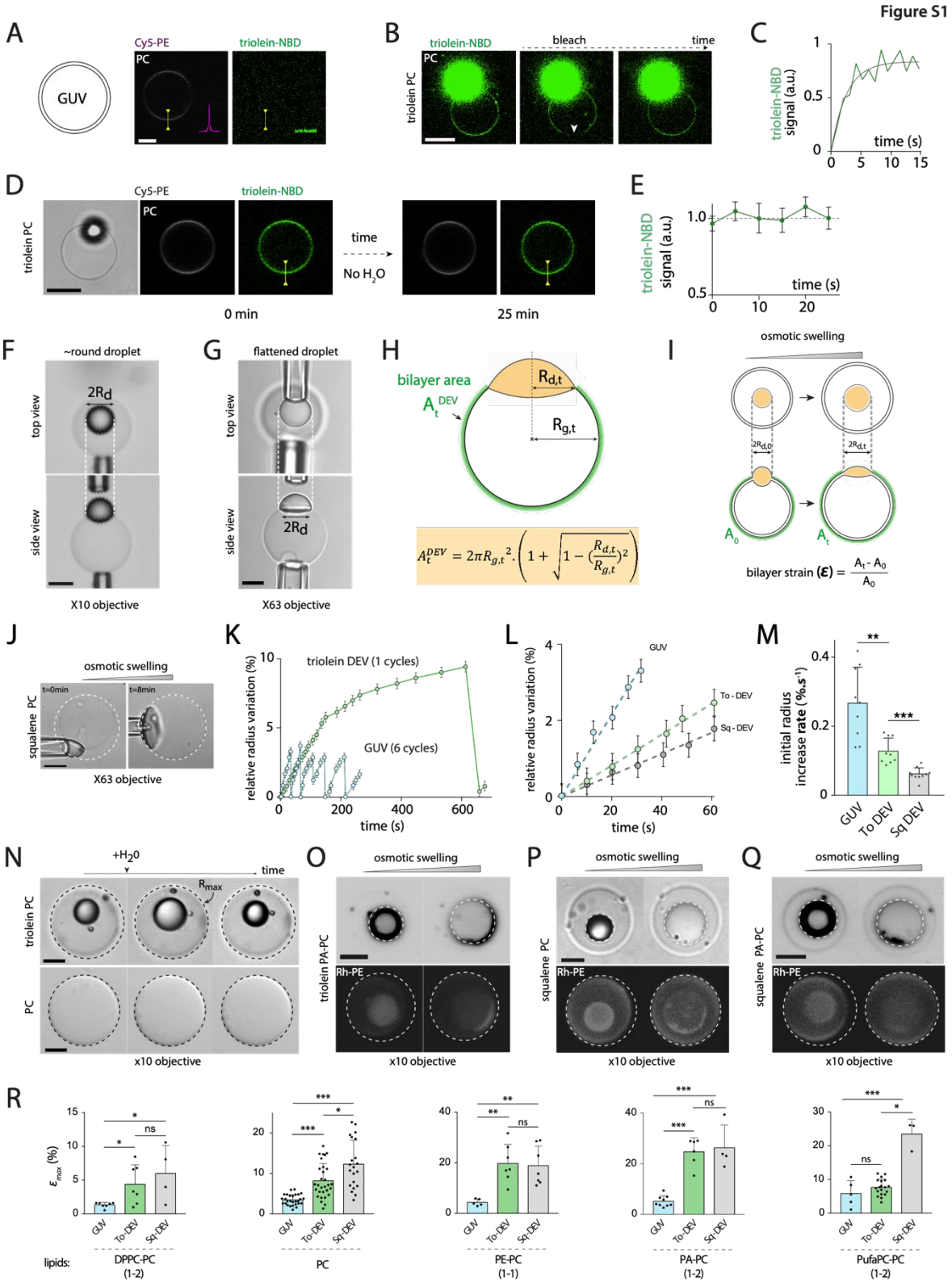

Figure S1: related to figure 1

A) Confocal images of a PC GUV marked with Cy5-PE. The same settings as in Figure 2B were used for the green channel. No signal of triolein-NBD was visible here. Scale bar: 5µm. **B)** Confocal images of PC DEVs of triolein supplemented with 0,05% (w/w) triolein-NBD to report for triolein distribution. Image sequence of a FRAP (Fluorescence Recovery After Photobleaching) experiment on the bilayer. After bleaching the bilayer (see arrowhead), the triolein-NBD signal recovered. The scale bar is 5µm. **C)** Over time quantification of normalized triolein-NBD fluorescence signal after bleaching showing recovery. The non-linear fit matches the FRAP recovery curve. The fit was done with an exponential "one-phase association model". **D)** Confocal images of PC DEVs of triolein supplemented with triolein-NBD. The triolein DEVs were imaged for 25 minutes with no osmotic shock. The scale bar is 10µm. **E)** Over time variations of the triolein NBD-signal in the bilayer shows no variation of triolein concentration during 25 minutes. Absolute value +/- measurement uncertainty. **F)** Confocal bright field images captured at x10 objective of single PC DEV of triolein at a low tension state. Top view and side view showing the same droplet radius (R_d) used to compute the initial bilayer area of a DEV. The scale bar is 10µm. **G)** Confocal bright field images captured at x63 objective of single PC DEV of triolein at a high tension state with a flattened droplet. Top view and side view showing the same droplet radius (R_d) used to compute the final bilayer area of a DEV. The scale bar is 5µm. **H) Top:** Illustration of a DEV and needed parameters to compute the DEV bilayer area subtracting the area occupied by the embedded droplet. **Bottom:** Equation used to compute the bilayer area of a DEV. **I) Top:** Schematic representation of the bilayer area variations during osmotic swelling of a DEV (top view and side view). Green arcs underly the bilayer area. **Bottom:** Equation used to compute the bilayer strain ε. **J)** Representative images of a PC squalene-DEV observed at x63 objective during a hypotonic shock experiment. The first image corresponds to the unswollen state and the second to one of the critical bilayer strain before burst. Dashed circles report maximum radius. Scale bar: 10µm. **K)** Related to Figure 1B. The plot of the relative vesicle radius variations of triolein DEV and GUV over time. Swelling and burst cycles are visible for GUVs (blue points; 6 cycles) and DEVs (green points; 1 cycle). Absolute value +/- measurement uncertainty. **L)** Plot of the vesicle relative radius variation at the beginning of a swelling experiment of a GUV (blue points), a triolein DEV (green points), and a squalene DEV (grey points). The slope of the linear fit (dotted lines on the graph) was used to determine the initial radius increase rate. Absolute value +/- measurement uncertainty. **M)** Plot of the initial radius increase rate of PC bilayer of GUVs (n=8), triolein-DEVs (n=9), and squalene DEVs (n=9). Mean +/- SD. **N)** Time-lapse of triolein DEV and GUV during a

hypotonic shock experiment. Black dashed circles report maximum radius. The scale bar is 5µm. **O)** Representative images of a PC-PA triolein-DEV during a hypotonic shock experiment. The first image corresponds to the unswollen state and the second to the bilayer critical strain before burst. Dashed circles report maximum radius. Scale bar: 10µm. **P)** Representative images of a PC squalene-DEV during a hypotonic shock experiment. The first image corresponds to the unswollen state and the second to the bilayer critical strain before burst. Dashed circles report maximum radius. Scale bar: 10µm. **Q)** Representative images of a PC-PA squalene-DEV during a hypotonic shock experiment. The first image corresponds to the unswollen state and the second to the bilayer critical strain before burst. Dashed circles report maximum radius. Scale bar: 10µm. **R)** Detailed plots of figure 1F. Critical bilayer strain is shown for each phospholipids conditions with a student t-test. Stars indicate if means are significantly different or not. Mean +/- SD.

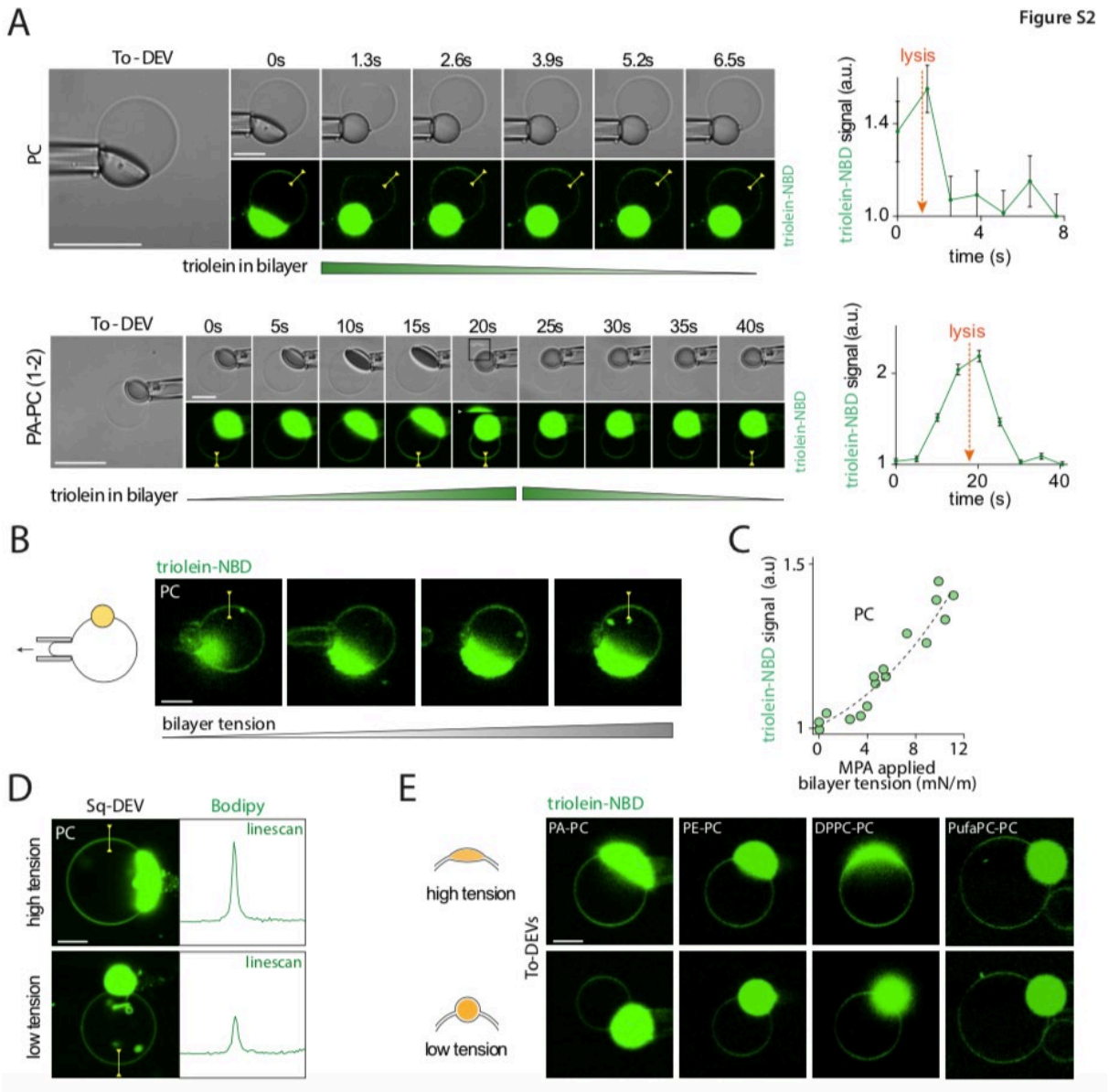

Figure S2: related to figure 2

A) Top: Time course of confocal images of a PC triolein-DEV (left) just after the burst of the vesicle. The scale bar is 20µm. Corresponding quantification of the amount of oil (right) in the bilayer shows a fast recovery of low triolein level after burst (few seconds). Absolute value +/- measurement uncertainty. **Bottom**: Time coarse of confocal images of a PC-PA triolein-DEV (left) before and after the burst. The scale bar is 20µm. Corresponding quantification of the amount of oil (right) in the bilayer shows a fast increase of oil level before burst followed by a rapid decrease of oil level after burst (few seconds). Absolute value +/- measurement uncertainty.

B) Left, Illustration of the method used to increase the bilayer tension of a triolein-DEV thanks to the micropipette aspiration technique. **Right**, the triolein-NBD signal in the bilayer of a PC triolein-DEVs during MPA-applied bilayer tension increase. Scale bar: 5µm. **C)** Plot of the triolein-NBD signal in bilayer against MPA-applied bilayer tension for PC triolein-DEVs. n=4 experiments. **D)** Confocal images of PC Sq-DEVs during the swelling experiment with bodipy, a hydrophobic probe. Scale bar: 5µm. A line scan of the bodipy signal in the bilayer is shown both in the stretched and unstretched state. **E)** Visualization of triolein-NBD signal in the bilayer during a hypotonic shock of PA-PC, PE-PC, DPPC-PC, and PufaPC-PC of triolein-DEVs both in the stretched and unstretched state. Scale bar: 5µm.

Figure S3

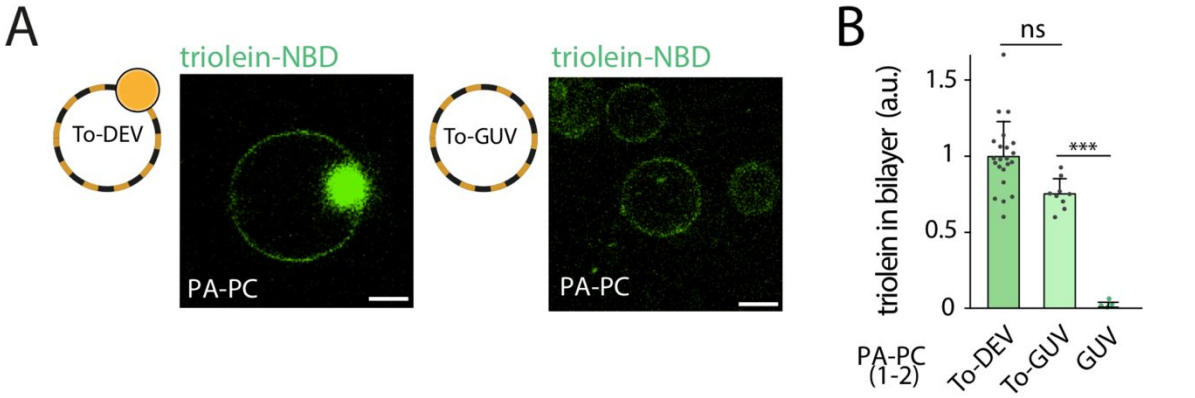
A
triolein-NBD
To-DEV
PA-PC
triolein-NBD
To-GUV
PA-PC
B
ns
***
triolein in bilayer (a.u.)
1.5
1
0.5
0
PA-PC (1-2)
To-DEV
To-GUV
GUV

Figure S3: related to figure 3

A) Confocal images of PA-PC triolein-DEV and triolein-GUV with triolein-NBD. Scale bar: 5µm. **B)** Plot of the triolein in bilayer for PC-PA GUVs (n=4), triolein-GUVs (n=9), and triolein-DEVs (n=22). Mean +/- SD.

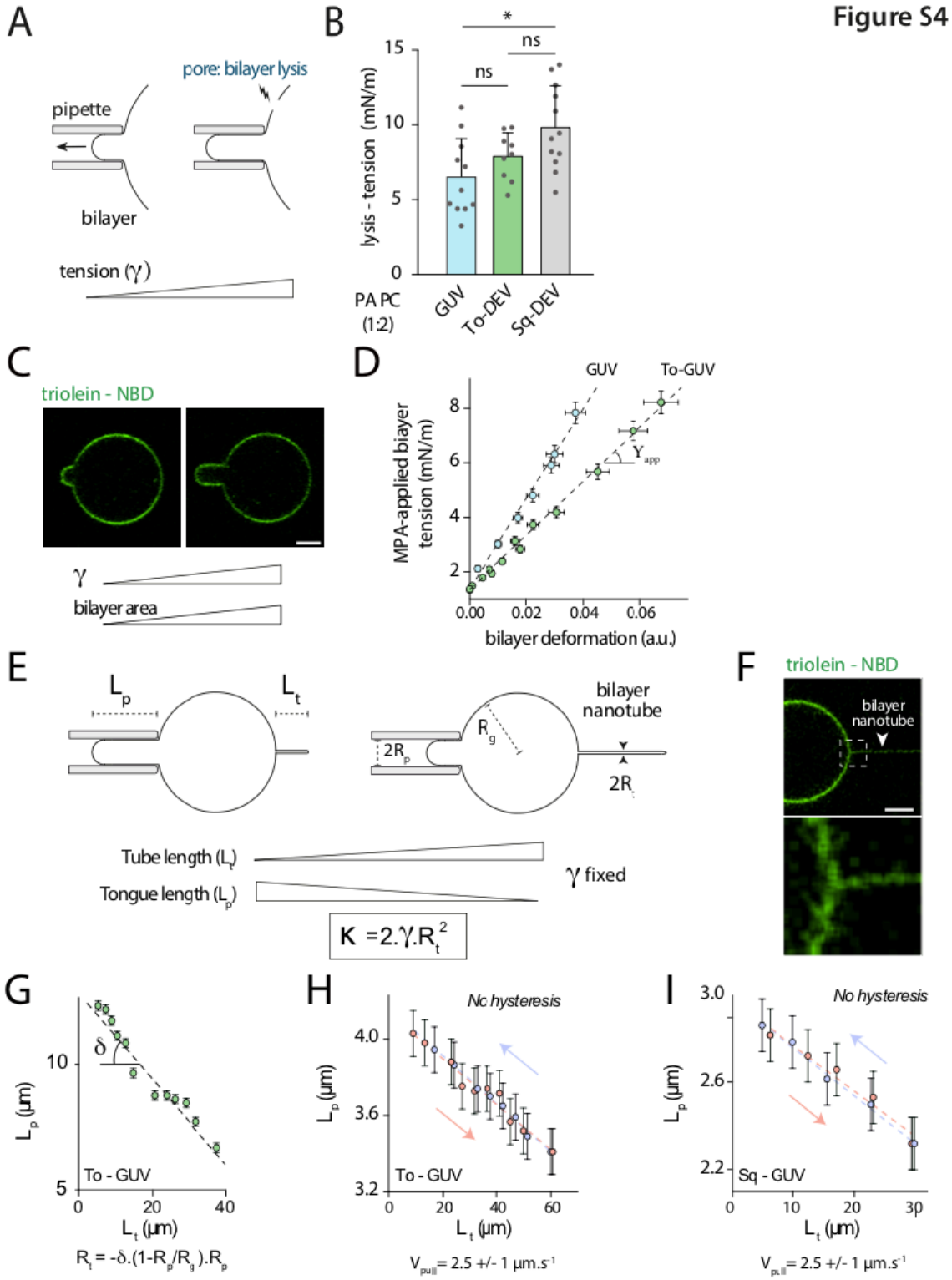
A
pore: bilayer lysis
pipette
bilayer
tension (γ)
B
*
ns
ns
lysis - tension (mN/m)
15
10
5
0
PA PC (1:2)
GUV
To-DEV
Sq-DEV
C
triolein - NBD
γ
bilayer area
D
GUV
To-GUV
MPA-applied biayer tension (mN/m)
8
6
4
2
0.00
0.02
0.04
0.06
bilayer deformation (a.u.)
E
L_p
L_t
2R_p
R_g
bilayer nanotube
2R_t
Tube length (L_t)
Tongue length (L_p)
γ fixed
K =2.γ.R_t^2
F
triolein - NBD
bilayer nanotube
G
δ
10
5
L_p (μm)
To - GUV
0
20
40
L_t (μm)
R_t = -δ.(1-R_p/R_g).R_p
H
Nc hysteresis
4.0
3.6
3.2
L_p (μm)
To - GUV
0
20
40
60
L_t (μm)
V_pull = 2.5 +/- 1 μm.s^-1
I
No hysteresis
3.0
2.6
2.2
L_p (μm)
Sq - GUV
0
10
20
3ρ
L_t (μm)
V_pull = 2.5 +/- 1 μm.s^-1

Figure S4: related to figure 4

A) Illustration of the method used for lysis tension determination. The bilayer tension of a vesicle is raised with a micropipette until the bilayer ruptures. Lysis tension is taken as the higher sustainable tension just before rupture. **B)** Membrane lysis tension of GUVs (n=11), triolein-DEVs (n=9) and squalene-DEVs (n=12) made with PC-PA. Mean +/- SD. **C)** Confocal images corresponding to the determination of the apparent area expansion modulus on a triolein-GUV with a triolein-NBD signal. Membrane tension is raised and the associated variation of the area is recorded. Scale bar: 5µm. **D)** Plot of the MPA-applied bilayer tension against area relative variation for a PC GUV (blue points) and a PC triolein-GUV (green points). Absolute value +/- measurement uncertainty. The slopes of the linear fits (dotted lines) are the elastic modulus of the corresponding GUV and triolein-GUV. **E)** Illustration of the determination protocol of the bending modulus computed with the membrane tension and the tube radius obtained by varying the tube length and recording the associated tongue length. **F)** Confocal images of a nanotube pulled from a PC triolein-DEV. Scale bar: 5µm. Zoom on the nanotube where a triolein-NBD signal is visible. Scale bar: 1µm. **G)** Example of a tongue length against tube length plot. The slope is linked with the nanotube radius which then allows computing the bending modulus. **H)** Tongue length against tube length plot for a triolein-GUV. The nanotube is pulled (red points) from the triolein-GUV and pushed (blue points) towards the triolein-GUV at a constant velocity of 2.5 +/- 1µm/s. Absolute value +/- measurement uncertainty. No hysteresis was detected indicating that oil partitioning is at the equilibrium during the tube pulling experiment. **G)** Tongue length against tube length plot for a squalene-GUV. The nanotube is pulled (red points) from the squalene-GUV and pushed (blue points) towards the squalene-GUV at a constant velocity of 2.5 +/- 1µm/s. Absolute value +/- measurement uncertainty. No hysteresis was detected indicating that oil partitioning is at equilibrium during the experiment.

Supplemental Text.

Supplementary materials: initial permeability determination for GUVs and DEVs

A. Fick law: conditions of utilization

Diffusion times of solutes through a phospholipid bilayer are negligible compared to the diffusion time of water. We therefore considered the diffusion of solutes through the bilayer of GUVs (or DEVs) as negligible compared to the diffusion of water. In this condition, Fick law leads to:

$$\frac{dV_t}{dt} = -\boldsymbol{P}.S_t.v_m.\Delta C(t)$$

where V_t is the volume inside the vesicle delimitated by S_t the area of permeation (ie area of bilayer), P the bilayer permeability to water, v_m the molar volume of water (18g.mol^{-1}) and $\Delta C(t)$ the difference of solutes concentration between the outside $C^e(t)$ and the inside $C^i(t)$ of the vesicle.

$$\Delta C(t) = C^e(t) - C^i(t)$$

B. $\Delta C(t)$: hypothesis and computation as a function of $R_{g,t}$

In our experiments, we considered only the first cycle of swelling and the first minute of experiment because it is difficult to characterize the concentration of solutes inside a GUV or a DEV after the first burst. We assume the concentration of solutes in the buffer to be constant and equal to the initial outside concentration C_0^e (145mOsm) as the buffer volume (220µL) is far greater than the volume of the vesicles having a radius between 5µm and 15µm (between 1pL and 15pL in volume). The concentration in the vesicle is equal to the initial one adjusted by the dilution factor $\frac{V_0}{V_t}$ where V_0 is the initial volume of the vesicle.

$$\Delta C(t) = C_0^e - C_0^i.\frac{V_0}{V_t} = C_0^i.(\frac{C_0^e}{C_0^i} - \frac{R_{g,0}^3}{R_{g,t}^3})$$

Where $R_{g,t}$ and $R_{g,0}$ are respectively the vesicle radius at the time t and at the beginning of swelling (**Figure 1**). As we have small variations of radius (<10%). We made the approximation that:

$$R_{g,t} = \delta R_{g,t} + R_{g,0}$$

where $\delta R_{g,t}$ represent the small variations of vesicle radius.

It follows that:

$$\Delta C(t) = C_0^i.\left(\frac{C_0^e}{C_0^i} - \frac{1}{(1+\frac{\delta R_{g,t}}{R_{g,0}})^3}\right)$$

At the first order we have:

$$\Delta C(t) = C_0^i.\left(\frac{C_0^e}{C_0^i} + \left(3\frac{\delta R_{g,t}}{R_{g,0}} - 1\right)\right)$$

Then we have:

$$\Delta C(t) = C_0^i.\left(\frac{C_0^e}{C_0^i} + 3\frac{R_{g,t}}{R_{g,0}} - 4\right)$$

Now that $\Delta C(t)$ is determine, in next, C&D, we will determine the exact surface and volume of DEV involve in the Fick law.

C. GUV and DEV permeation surface: hypothesis and computation as a function of $\mathbf{R_{g,t}}$

The permeation surface of the GUV (S_t^{GUV}) corresponds to the surface of the sphere formed by its bilayer and can be expressed as:

$$S_t^{GUV} = 4\pi {R_{g,t}}^2$$

In the case of the DEV, the water cannot pass through the oil droplet. Thus to assess the permeation surface of a DEV (S_t^{DEV}) we have to subtract the surface area occupied by the droplet S_t^{cap} from the surface area of the sphere forming its bilayer S_t^{GUV} (see **Figure 1**) :

$$S_t^{DEV} = S_t^{GUV} - S_t^{cap}$$

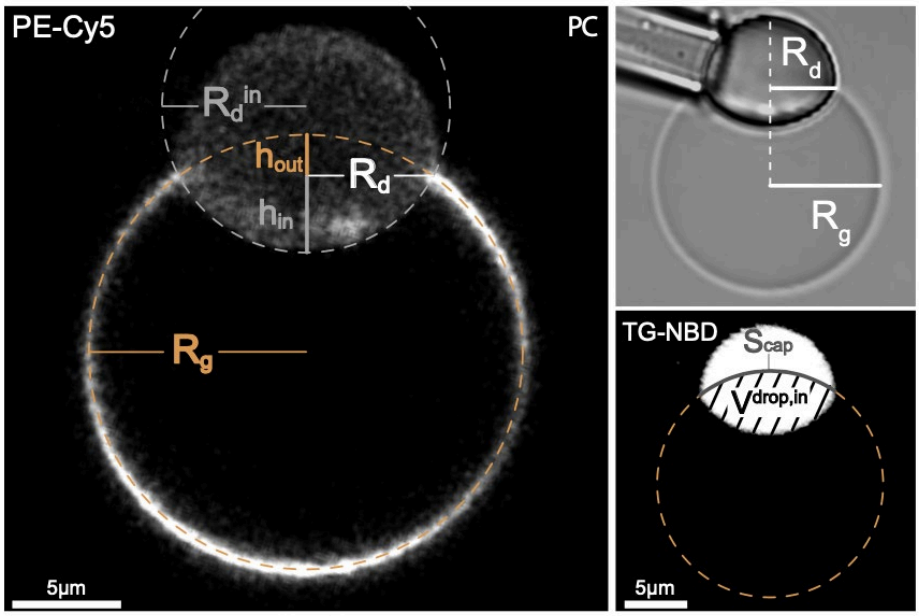

Figure 1: triolein-DEVs of DOPC at x63 objective showing parameters to compute the corrected surface and volume of a DEV.

Note that both S_t^{cap} and S_t^{GUV} (**Figure 1**) are varying over time due to the variations of the vesicle $R_{g,t}$ and the droplet radii $R_{d,t}$ (**Figure 2**).

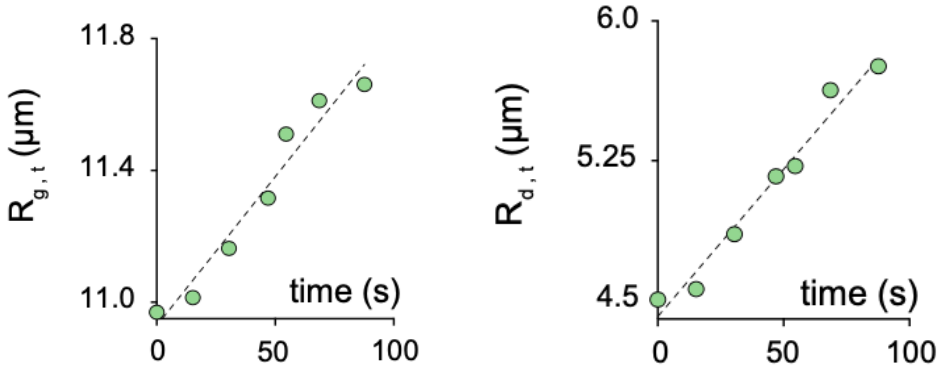

Figure 2: Plot of R_g and R_d as a function of time

S_t^{cap} can be calculated as follow:

$$S_t^{cap} = 2\pi {R_{g,t}}^2 . \left(1 - \sqrt{1 - (\frac{R_{d,t}}{R_{g,t}})^2}\right)$$

Following, we have S_t^{DEV}:

$$S_t^{DEV} = 2\pi {R_{g,t}}^2 . \left(1 + \sqrt{1 - (\frac{R_{d,t}}{R_{g,t}})^2}\right)$$

Compared to an equivalent droplet-free vesicle, the permeation area of the DEV must therefore be corrected by the following factor:

$$\beta_t = \frac{S_t^{DEV}}{S_t^{GUV}} = \frac{1}{2}\left(1 + \sqrt{1 - (\frac{R_{d,t}}{R_{g,t}})^2}\right)$$

Correction factor β_t:

As the radius of the vesicle ($R_{g,t}$) and the radius of the droplet ($R_{d,t}$) evolved during the osmotic swelling (**Figure 2**), we calculated β_t over time and found that it only varied from 0,922 to 0,899. These variations are represented in **Figure 3**.

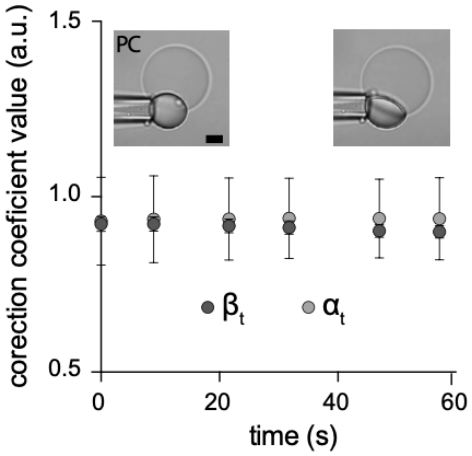

Figure 3: Plot of the correction coefficient α and β

In order to better quantify this small decrease of β_t , we calculated the ratio between the initial β_t and its value after 60 second of each osmotic swelling experiment (β_{60}/β_0, Figure 4, right). We find that β_t has very small variations: $2{,}15 \pm 0.67$ % and $1{,}04 \pm 0.69$ % respectively for To-DEV and Sq-DEV (**Figure 4, right**). Based on these observations, we considered $\beta_t = \beta_0$. We plotted all the value of β_0 in (**Figure 4, left**).

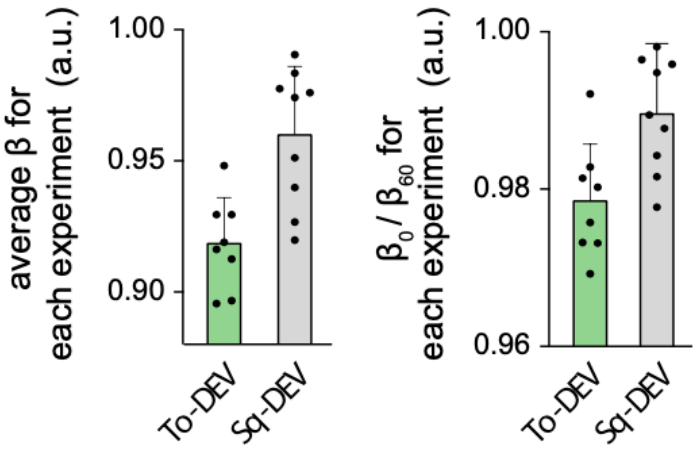

$$S_t^{DEV} = 4\pi R_{g,t}^2 . \beta_0$$

Figure 4: Left: Mean value of β for DEVs permeability assay; Right: Variations of β during permeability experiment.

We thus have a surface of permeation S_t which can written as:

$$S_t = \beta_0 . 4\pi {R_{g,t}}^2 \text{ for DEV and } S_t = 4\pi {R_{g,t}}^2 \text{ for GUVs}$$

D. GUV and DEV volume: hypothesis and computation as a function of $R_{g,t}$

For the volume of a GUV, V_t can be expressed as:

$$V_t^{GUV} = \frac{4}{3}\pi {R_{g,t}}^3$$

The inside DEV volume V_t^{DEV} has to be corrected because of the presence to the droplet:

$$V_t^{DEV} = V_t^{GUV} - V_t^{drop,in}$$

where $V_t^{drop,in}$ is the lacking of aqueous volume in the vesicle occupied by the embedded droplet (see Figure S1A). V_t^{DEV} can be expressed as:

$$V_t^{DEV} = \frac{4}{3}\pi {R_{g,t}}^3 - \frac{\pi}{3}(h_{out,t}^2(3R_{g,t} - h_{out,t}) + (h_{in,t}^2(3R_{drop,t}^{in} - h_{in,t})$$

where $h_{out,t}$, $h_{in,t}$ and $R_{drop,t}^{in}$ are all defined in **Figure 1**.

It follows:

$$\frac{V_t^{DEV}}{V_t^{GUV}} = 1 - \frac{(h_{out,t}^2(3R_{g,t} - h_{out,t}) + (h_{in,t}^2(3r_{drop,t}^{in} - h_{in}, t)}{4R_{g,t}^3} = \alpha_t$$

For the experiment in **figure 2** the variation of α_t are plotted as a function of time (**Figure 3**).

Correction factor α_t:

Where α_t is the correction factor of the DEV inner volume compared to the one of GUVs. As we did previously for β_t , α_t is plotted as a function of time (Figure 3). The variation of α_t is also very small, from 0,930 to 0,937. We also examined for each experiment the variations of α_t during the first 60 seconds α_{60}/α_0 (Figure 5, right) which were very small: $1{,}11 \pm 0.35\,\%$ and $0{,}50 \pm 0.48\,\%$ respectively for To-DEV and Sq-DEV (**Figure 5, right**). Based on these observations, we considered $\alpha_t = \alpha_0$. We plotted all the value of α_0 in (**Figure 5 left**).

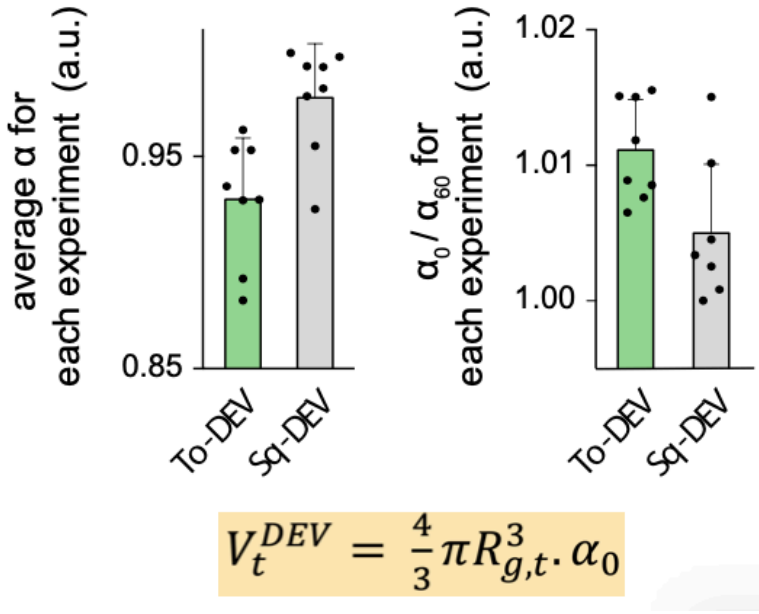

$$V_t^{DEV} = \frac{4}{3}\pi R_{g,t}^3 . \alpha_0$$

Figure 5: Left: Mean value of α for DEVs permeability assay; Right: Variations of α during permeability experiment.

In conclusion, the volume of permeation of a DEV and a GUV write as:

$$V_t = \alpha_0 . \frac{4}{3}\pi {R_{g,t}}^3 \quad \text{for DEVs and} \quad V_t = \frac{4}{3}\pi {R_{g,t}}^3 \quad \text{for GUVs}$$

E. Fick law with $R_{g,t}$ as the sole variable:

Considering the expression $\Delta C(t)$ established in B. one obtains:

$$\frac{dV_t}{dt} = -P . S_t . v_m . C_0^i . \left(\frac{C_0^e}{C_0^i} + 3\frac{R_{g,t}}{R_{g,0}} - 4 \right)$$

Replacing V_t *and* S_t by their expression obtained in C. and D leads to:

$$\frac{d(\alpha_0 . \frac{4}{3}\pi {R_{g,t}}^3)}{dt} = -P . \beta_0 . 4\pi {R_{g,t}}^2 . v_m . C_0^i . \left(\frac{C_0^e}{C_0^i} + 3\frac{R_{g,t}}{R_{g,0}} - 4 \right)$$

We obtain a differential equation of the first order with a constant second member:

$$\frac{d(\frac{R_{g,t}}{R_{g,0}})}{dt} + \frac{3P.\beta_0.\alpha_0^{-1}.v_m.C_0^i}{R_{g,0}}\frac{R_{g,t}}{R_{g,0}} = \frac{P.\beta_0.\alpha_0^{-1}.v_m.C_0^i}{R_{g,0}}.\left(4 - \frac{C_0^e}{C_0^i}\right)$$

So:

$$\frac{d\left(\frac{R_{g,t}}{R_{g,0}}\right)}{dt} + a\frac{R_{g,t}}{R_{g,0}} = \frac{a}{3}\left(4 - \frac{C_0^e}{C_0^i}\right) \quad \text{where} \quad a = \frac{3P.\beta_0.\alpha_0^{-1}.v_m.C_0^i}{R_{g,0}}$$

As we have linear curve for $\frac{R_{g,t}}{R_{g,0}}$ for the first 60 seconds (**Figure S1L**), $\frac{d\left(\frac{R_{g,t}}{R_{g,0}}\right)}{dt} = \omega$ is constant and equal to the slope of $\frac{R_{g,t}}{R_{g,0}}$.

$$\omega = (\left(4 - \frac{C_0^e}{C_0^i}\right) - 3\frac{< R_{g,t} >}{R_{g,0}})\frac{P_{initial}.\beta_0.\alpha_0^{-1}.v_m.C_0^i}{R_{g,0}}$$

Here, $P_{initial}$, "initial permeability" replaces the permeability because we considered only initial slope at the beginning of experiment. For a given experiment, $< R_{g,t} >$ is the mean of $R_{g,t}$ in the first 60 seconds.

$$P_{initial} = \frac{\omega.R_{g,0}}{\beta_0.\alpha_0^{-1}.v_m.((4-3\frac{<R_{g,t}>}{R_{g,0}})C_0^i - C_0^e)}$$

With this expression, we determined the initial permeability to water $P_{initial}$ for PC GUVs, PC triolein-DEVs and PC squalene-DEVs. (**Principal Figure 1E, left**)

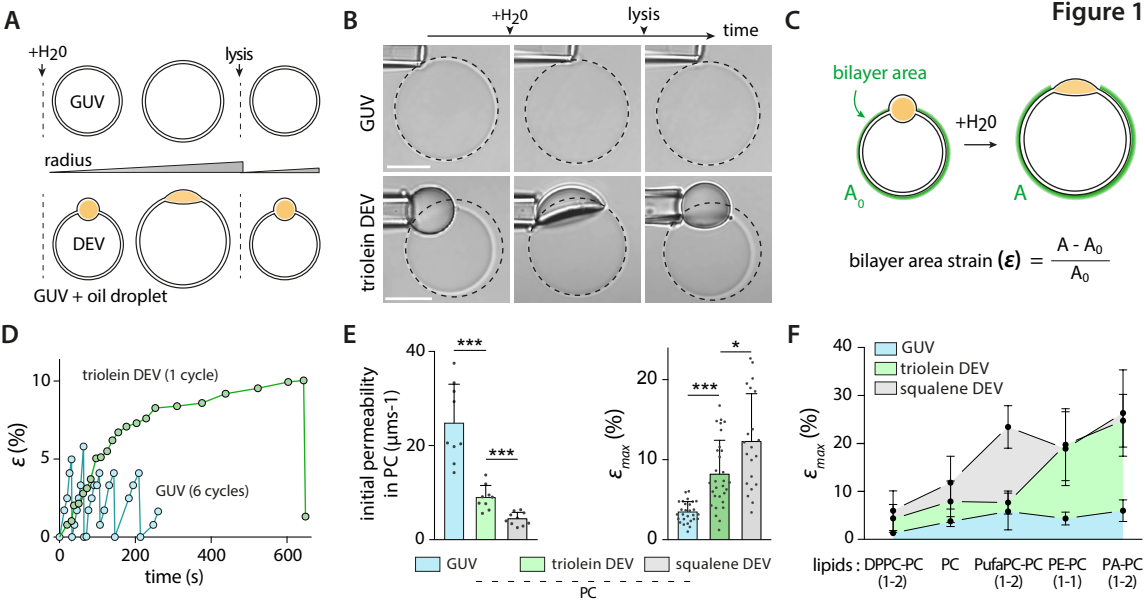
Figure 1
A
+H20
lysis
GUV
radius
DEV
GUV + oil droplet
B
+H20
lysis
time
GUV
triolein DEV
C
bilayer area
+H20
A0
A
bilayer area strain (ε) = (A - A0) / A0
D
triolein DEV (1 cycle)
GUV (6 cycles)
ε (%)
time (s)
E
initial permeability in PC (µms-1)
***
***
GUV
triolein DEV
squalene DEV
PC
εmax (%)
***
*
F
GUV
triolein DEV
squalene DEV
εmax (%)
lipids : DPPC-PC (1-2)
PC
PufaPC-PC (1-2)
PE-PC (1-1)
PA-PC (1-2)

Figure 2

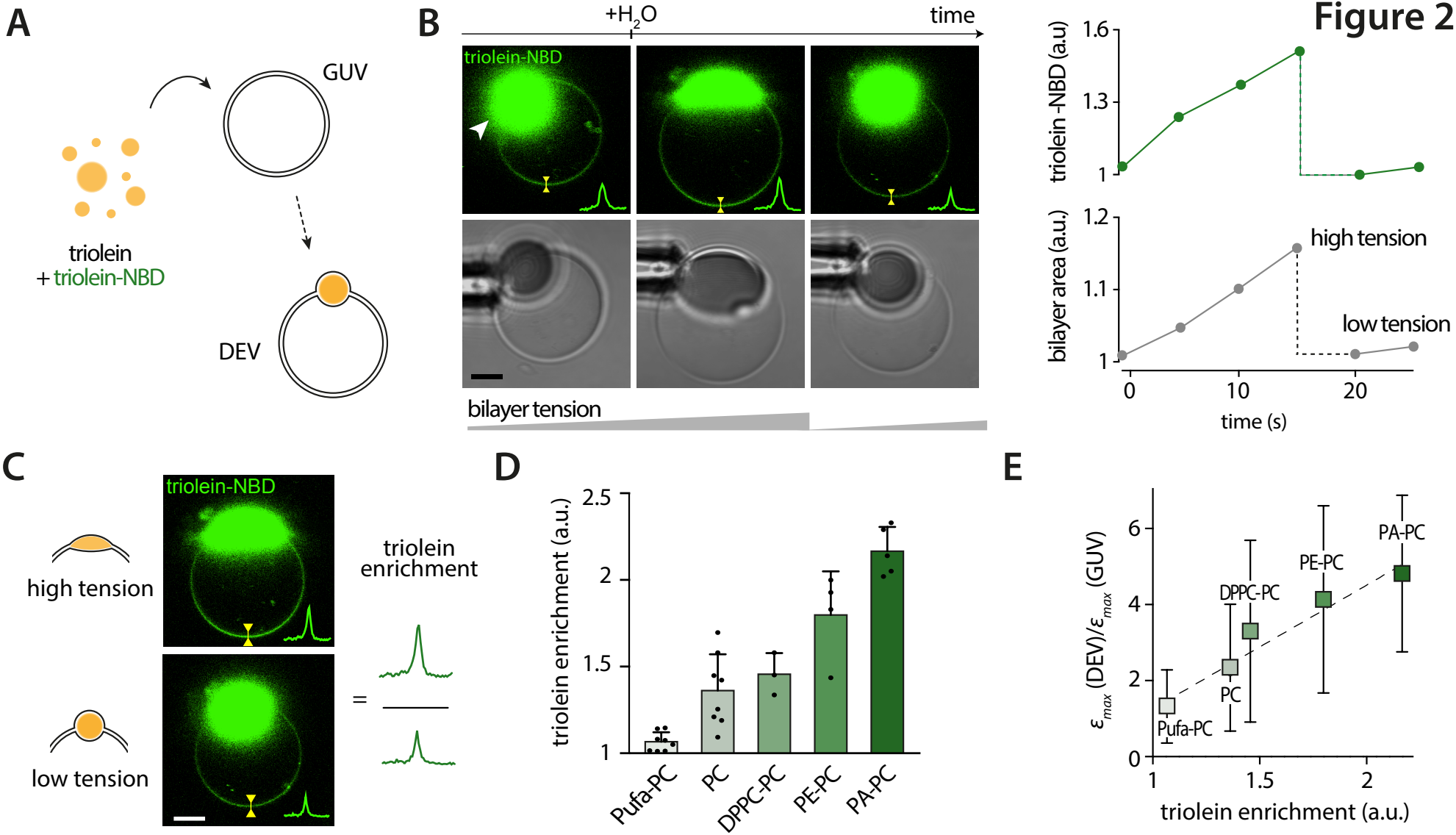
A
GUV
triolein
+ triolein-NBD
DEV
B
+H2O
time
triolein-NBD
bilayer tension
triolein -NBD (a.u.)
1.6
1.3
1
bilayer area (a.u.)
1.2
1.1
1
high tension
low tension
0
10
20
time (s)
C
triolein-NBD
high tension
low tension
=
triolein
enrichment
D
triolein enrichment (a.u.)
2.5
2
1.5
1
Pufa-PC
PC
DPPC-PC
PE-PC
PA-PC
E
εmax (DEV)/εmax (GUV)
6
4
2
0
Pufa-PC
PC
DPPC-PC
PE-PC
PA-PC
1
1.5
2
triolein enrichment (a.u.)

Figure 3

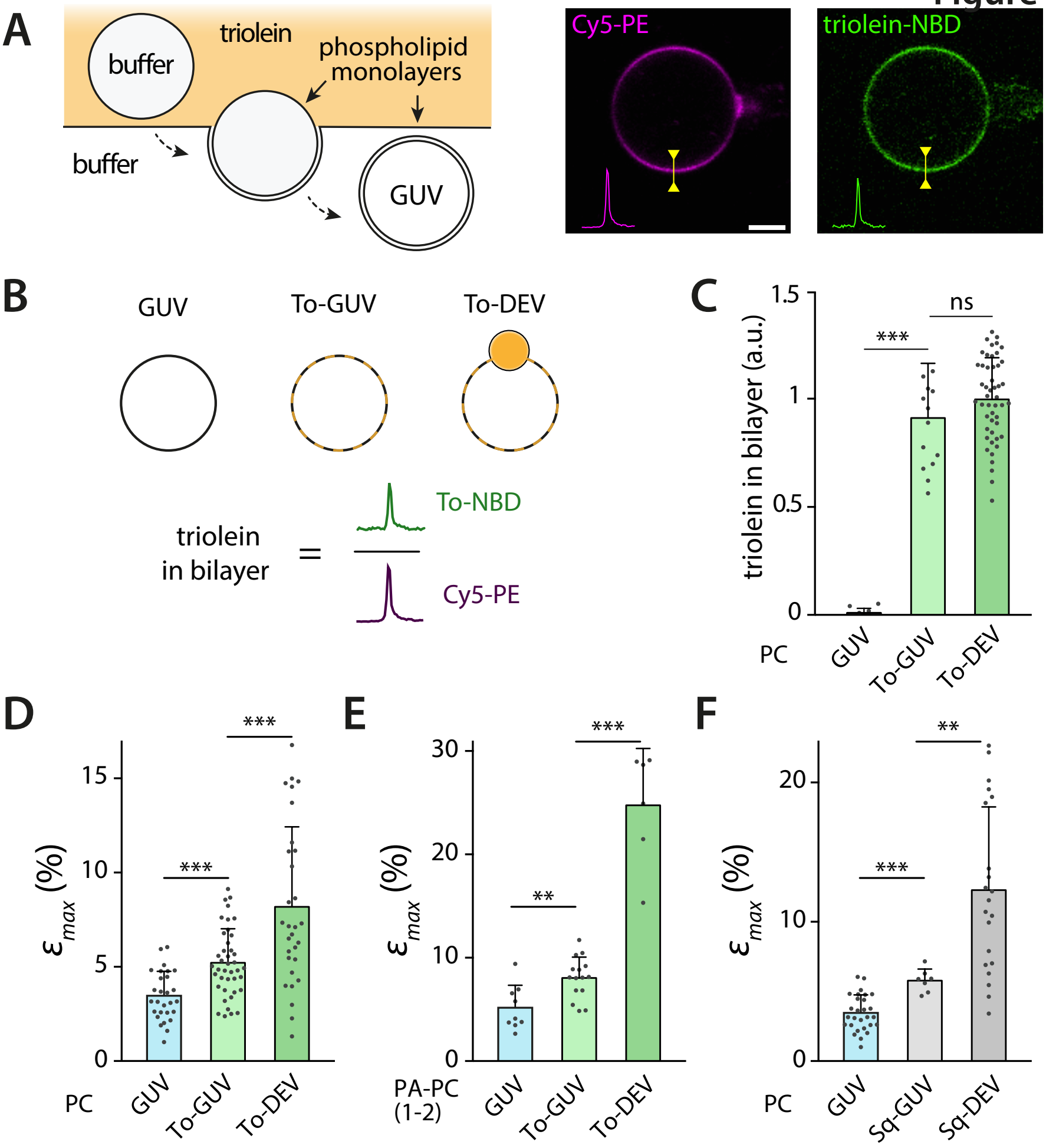
A
buffer
triolein
phospholipid monolayers
buffer
GUV
Cy5-PE
triolein-NBD
B
GUV
To-GUV
To-DEV
triolein in bilayer
=
To-NBD
Cy5-PE
C
triolein in bilayer (a.u.)
1.5
1
0.5
0
ns
***
PC
GUV
To-GUV
To-DEV
D
ε_{max} (%)
15
10
5
0
***
***
PC
GUV
To-GUV
To-DEV
E
ε_{max} (%)
30
20
10
0
***
**
PA-PC (1-2)
GUV
To-GUV
To-DEV
F
ε_{max} (%)
20
10
0
**
***
PC
GUV
Sq-GUV
Sq-DEV

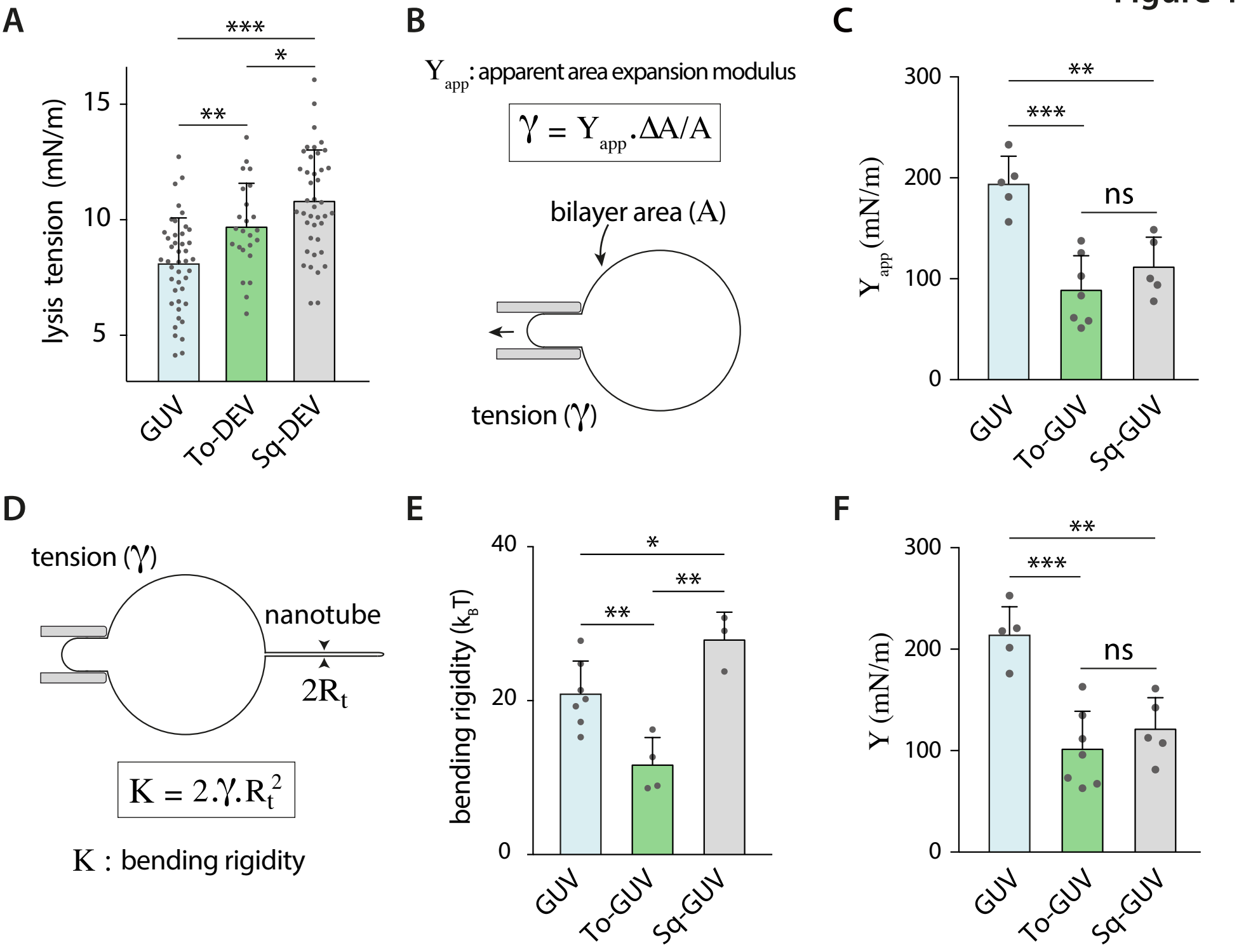
A
lysis tension (mN/m)
15
10
5
***
*
**
GUV
To-DEV
Sq-DEV
B
Y_{app}: apparent area expansion modulus
$\gamma = Y_{app}.\Delta A/A$
bilayer area (A)
tension (γ)
C
Y_{app} (mN/m)
300
200
100
0
**
***
ns
GUV
To-GUV
Sq-GUV
D
tension (γ)
nanotube
$2R_t$
$K = 2.\gamma.R_t^2$
K : bending rigidity
E
bending rigidity (k_BT)
40
20
0
*
**
**
GUV
To-GUV
Sq-GUV
F
Y (mN/m)
300
200
100
0
**
***
ns
GUV
To-GUV
Sq-GUV